


2014-01-01

Nanometric Structure-Property Relationship in Hafnium Oxide Thin Films Made by Sputter-Deposition

Mirella Vargas

University of Texas at El Paso, mvargas8@miners.utep.edu

Follow this and additional works at: https://digitalcommons.utep.edu/open_etd

 Part of the [Materials Science and Engineering Commons](#), [Mechanical Engineering Commons](#), and the [Mechanics of Materials Commons](#)

Recommended Citation

Vargas, Mirella, "Nanometric Structure-Property Relationship in Hafnium Oxide Thin Films Made by Sputter-Deposition" (2014). *Open Access Theses & Dissertations*. 1369.
https://digitalcommons.utep.edu/open_etd/1369

This is brought to you for free and open access by DigitalCommons@UTEP. It has been accepted for inclusion in Open Access Theses & Dissertations by an authorized administrator of DigitalCommons@UTEP. For more information, please contact lweber@utep.edu.

NANOMETRIC STRUCTURE-PROPERTY RELATIONSHIP IN
HAFNIUM OXIDE THIN FILMS MADE BY SPUTTER-DEPOSITION

MIRELLA VARGAS

Department of Metallurgical and Materials Engineering

APPROVED:

Chintalapalle V. Ramana, Ph.D., Chair

Stephen W. Stafford, Ph.D.

David A. Roberson, Ph.D.

Bess Sirmon-Taylor, Ph.D.

Interim Dean of the Graduate School

Copyright ©

by

Mirella Vargas

2014

Dedication

This thesis is lovingly dedicated to my mother for her invaluable wisdom from which she taught me to love school.

NANOMETRIC STRUCTURE-PROPERTY RELATIONSHIP IN HAFNIUM
OXIDE THIN FILMS MADE BY SPUTTER-DEPOSITION

by

Mirella Vargas, B.S. MME

MASTER'S THESIS

Presented to the Faculty of the Graduate School of

The University of Texas at El Paso

in Partial Fulfillment

of the Requirements

for the Degree of

MASTER OF SCIENCE

Department of Metallurgical and Materials Engineering

THE UNIVERSITY OF TEXAS AT EL PASO

May 2014

Acknowledgements

I would like to express my sincere and utmost appreciation to Dr. C.V. Ramana, for allowing me to work under his advising and entrusting me with his research for the accomplishment of this thesis for my Master's degree. I want to acknowledge the faculty of the Department of Metallurgical and Materials Engineering at *UTEP* for their profound knowledge and distinct backgrounds in various disciplines. In addition, I would like to thank Dr. Angela Campbell for exposing me to a national laboratory setting at The Air Force Research Lab in Dayton, OH. I am appreciative of the research team I am a part of and the dynamic that Dr. Ramana has established among us. I am thankful to coworkers former and present: Dr. Christopher Bradley, Christian Barraza, Gustavo Martinez, and Ernesto J. Rubio. A sincere thank you is due to Mr. David Brown for his technical support and intelligence far greater than any Ivy League graduate.

It would not be fair to submit this documentation without the mention of my officemates and classmates. The outcome of my career and future endeavors has been greatly influenced by the friendship of Brenda Arellano, Mayra Contreras, and Amanda Gutierrez. The late nights spent in the office deciphering Dr. Murr's homework were far more pleasant and lively than any leisurely late night. Lastly, I extend my gratitude to close friends and family for their unparalleled love and support.

Abstract

Hafnium oxide (HfO_2) is technologically an important material, which exhibits a unique set of properties such as a high dielectric constant ($k \sim 25$) and wide band gap (~ 5.7 eV) which make this material attractive in the fields of microelectronics and optoelectronics. HfO_2 has become the leading candidate to replace SiO_2 dielectrics in gate oxides due to a higher permittivity and reportedly lower electron tunneling effects. HfO_2 exhibits various polymorphs; the thermodynamic stability and phase existence depends on the temperature and pressure conditions. In addition, the controlled growth and manipulation of specific HfO_2 crystal structures at the nanoscale dimensions is the driving force for current and emerging technological implications. Therefore, it is important to characterize and obtain a correlation between physio-chemical and optical properties in nanocrystalline HfO_2 films as a function of growth conditions. The present work entails a detailed analysis of growth behavior, microstructure, and optical properties of monoclinic HfO_2 films as a function of growth temperature. Amorphous and nanocrystalline HfO_2 films were grown by sputter-deposition by varying deposition temperature (T_s) in a wide range from 25-700 °C. Characterization of the films employing an array of analytical techniques indicate a clear functional relationship between processing conditions, structure, morphology, and optical properties. HfO_2 films were amorphous at $T_s \leq 200$ °C, at which point a structural transformation occurs. HfO_2 films grown at $T_s \geq 200$ °C were nanocrystalline, stabilized in a monoclinic structure. The nanocrystalline HfO_2 films exhibit a strong ($\bar{1} 11$) texturing. The average crystallite size of HfO_2 films increased from ~ 10 nm to ~ 20 nm with increasing T_s . Electron and atomic force microscopy measurements also correlated with the crystalline behavior, as well as an evenly distributed network of crystals spherical in shape for the nano-crystalline films. Density of HfO_2 films probed using X-ray

reflectivity and ellipsometry data analysis indicate that the values vary in the range of 7.36-9.14 g/cm³. The higher end of the density values were noted only for HfO₂ films grown at relatively higher T_s. The band gap values of the films vary in the range of 5.75-6.19 (±0.03) eV for T_s=25-700 °C. Index of refraction at 550 nm increased from 1.80 to 2.09, which also correlates with the characteristic feature of improved structural order.

Table of Contents

Acknowledgements	v
Abstract	vi
List of Tables	x
List of Figures	xi
Chapter 1: Introduction	1
1.1 Polymorphisms of HfO ₂	1
1.2 Properties of HfO ₂ Thin Films	4
1.2.1 Optical Nature	5
1.2.2 CMOS Technology and Electronic Properties	7
1.2.3 Mechanical Behavior	11
1.3 Fabrication Techniques	11
Chapter 2: Literature Review	14
2.1 Literature Review	14
2.2 Motivation	18
Chapter 3: Experimental Details	19
3.1 Film Fabrication	19
3.2 Film Characterization	21
3.2.1 X-Ray Diffraction (XRD)	21
3.2.2 Scanning Electron Microscopy (SEM)	23
3.2.3 Atomic Force Microscopy (AFM)	24
3.2.4 X-Ray Reflectivity (XRR)	26
3.2.5 Spectrophotometry Measurements	28
3.2.6 Spectroscopic Ellipsometry (SE)	29
Chapter 4: Results & Discussion	32
4.1 Crystal Structure	32
4.2 Film Thickness and Density	34
4.3 Surface Morphology	39
4.4 Spectral Transmission Characteristics and Band Gap	44
4.5 Optical Constants	49
Chapter 5: Conclusion	57
Chapter 6: Future Work	58

Vita.....	67
-----------	----

List of Tables

Table 1.1: Summarized characteristics and mechanical properties of bulk HfO ₂	11
Table 4.1: Fit parameters generated by using GlobalFit (Reflectivity Analysis)	38
Table 4.2: Mean-squared error values from the quality of the match between the data calculated from the model and the experimental data.....	54

List of Figures

Figure 1.1: Unit cells of HfO ₂ structures along with unit cell parameters (a) monoclinic unit cell, P2 ₁ /C; (b) tetragonal unit cell, P4 ₂ /nmc; (c) cubic unit cell, Fm3m; (d) orthorhombic I unit cell, Pbc _a ; (e) orthorhombic II unit cell, Pnma.....	3
Figure 1.2: Phase diagram for the Hafnium-Oxygen system, indicating the proposed temperature dependent phases of HfO ₂	4
Figure 1.3: Variation of dielectric constant with band gap. The choice for high- <i>K</i> materials becomes limited since there is a contraindication with band gap selection.....	9
Figure 1.4: (a) Band diagrams of hafnium-based materials on Si and (b) band diagrams of HfO ₂ on different semiconductors for potential applications into Si advance technologies as well as non-silicon based devices.	10
Figure 1.5: Deposition technique flow chart for HfO ₂ depicting the pros and cons of typical fabrication methods.....	13
Figure 3.1: Principle of an rf sputtering system, demonstrating the role of the magnetic field ...	20
Figure 3.2: Sputtering system employed for the growth of the HfO ₂ films.....	21
Figure 3.3: Bruker D8 advanced diffractometer used for GIXRD scans.....	23
Figure 3.4: Hitachi S4800 SEM.....	24
Figure 3.5: Schematic representation of an AFM instrument configuration	26
Figure 3.6: Reflection and refraction of X-rays on a material surface	27
Figure 3.7: Schematic representation of X-ray incident beam when the incident angle is less than the critical angle.....	27
Figure 3.8: Structural information provided by X-ray reflectivity profile.....	28
Figure 3.9: Cary 5000 spectrophotometer.	29

Figure 3.10: J.A. Woollam WVASE ellipsometer.....	31
Figure 4.1: (a) GIXRD scans for HfO ₂ films grown by variable temperature (b) High resolution scans of the ($\bar{1}11$) peaks obtained to assess further structural information.....	33-34
Figure 4.2: Crystallite size, FWHM, and <i>d</i> -spacing values obtained by fitting the high resolution ($\bar{1}11$) peaks with a Gaussian distribution.	34
Figure 4.3: Cross-sectional imaging of the films obtained through electron microscopy to estimate direct film thickness.....	36
Figure 4.4: Layer model representative of the HfO ₂ films constructed for XRR data analysis. ..	36
Figure 4.5: XRR spectra including experimental and model curves for the HfO ₂ films grown at T _s =300-700 °C.	37
Figure 4.6: Density profile, thickness, and roughness values determined from XRR spectra for the crystalline HfO ₂ films grown at T _s = 300 - 700 °C.....	38
Figure 4.7: SEM surface images for the HfO ₂ films grown as a function of T _s ; the polycrystalline films all entertain an equiaxed grain morphology at the nanoscale.....	39-40
Figure 4.8: AFM surface images for the polycrystalline set of HfO ₂ thin films; the crystallite morphology correlates with SEM.	41-42
Figure 4.9: 3D AFM images demonstrating an overall decrease in surface height with increasing T _s	42-43
Figure 4.10: Roughness profile obtained by AFM imaging; superimposed are XRR roughness measurements for T _s = 300 – 700 °C.....	44
Figure 4.11: Transmission spectra for the HfO ₂ films.	46
Figure 4.12: Absorption coefficient, α , as a function of photon energy for HfO ₂ films.....	47
Figure 4.13: $(\alpha h\nu)^2$ as a function of photon energy for the HfO ₂ films grown at T _s = RT – 600 °C.	47-48

Figure 4.14: Summarized band gap values as a function of T_s	48
Figure 4.15: Optical stack model employed for SE data analysis.	51
Figure 4.16: The spectral dependencies of Ψ and Δ along with the simulated data constructed from the optical model for HfO_2 films.	52-54
Figure 4.17: Film thickness measurements, measured directly through SEM, and by data fitting for XRR and SE analysis.	54
Figure 4.18: Index of refraction as a function of wavelength (300 – 1350 nm).	55
Figure 4.19: ‘ n ’ values extracted at $n(550)$ to understand as a function of T_s	55
Figure 4.20: Density measurements approximated through the Lorentz-Lorenz relation and compared to XRR derived measurements.....	56

Chapter 1: Introduction

Hafnium oxide (HfO_2) is a technologically important metal oxide, which is characterized by a unique combination of mechanical, chemical, electronic and optical properties [1-30]. HfO_2 films exhibit a high dielectric constant ($k \sim 25$) and a wide band gap ($E_g \sim 5.7$ eV), which makes the material attractive for applications in the fields of electronics and opto-electronics [3,11]. HfO_2 remains the leading candidate to replace SiO_2 dielectrics in gate oxides due to a higher permittivity and reportedly lower electron tunneling effects [5,6].

HfO_2 exhibits various polymorphs; the thermodynamic stability and phase existence depends on the temperature and pressure conditions. In addition, the controlled growth and manipulation of specific HfO_2 crystal structures at the nanoscale dimensions is the driving force for current and emerging technological implications. Tailoring film properties ultimately decides the ideal device application; optimizing device performance requires a detailed understanding of the geometric structure, particularly at the nanoscale level. Therefore, it is important to characterize and obtain a correlation between structure and optical properties in nanocrystalline hafnium oxide (HfO_2) films as a function of growth conditions. The remainder of this chapter is aimed at introducing the material characteristics and significant aspects of HfO_2 in order to understand the derivation of a structure-property relationship at the nanoscale dimensions, which is the primary focus of this research work.

1.1 Polymorphisms of HfO_2

The phase existence is dependent upon several of the synthesis/processing variables, viz., pressure, temperature, impurity/dopant content, growth conditions, and interfacial strain [1]. The phase stability discussion considering the phase transformations of bulk HfO_2 based on temperature and pressure provides a fundamental knowledge when specifically considering the

crystallographic aspects of thin films and nanomaterials. At ambient conditions, HfO_2 crystallizes in the monoclinic baddeleyite structure belonging to the space group $P2_1/C$ [2]. Monoclinic HfO_2 has four molecules per unit cell and when exposed to oxygen and ambient conditions hafnium bonds to oxygen and becomes seven fold-coordinated as shown in Figure 1.1a [3]. Monoclinic HfO_2 possesses the lowest free energy of formation and the largest volume [1,3]. An increase in temperature transforms the monoclinic structure into tetragonal HfO_2 at 1743 °C with space group $P4_2/nmc$ (Fig. 1.1b). Further increase in temperature to 2500 °C results in the cubic phase formation of HfO_2 . Cubic HfO_2 is of a calcium fluorite (CaF_2) structure belonging to space group $Fm3m$ (Fig. 1.1c). The hafnium atoms are in the face-centered cubic (fcc) structure and the oxygen atoms occupy the tetrahedral interstitial sites associated with the fcc lattice, whereas tetragonal HfO_2 can be viewed as a distortion of the cubic structure obtained by displacing alternating pairs of oxygen atoms up and down [5]. The transformation between the temperature induced phases is highly associated with the change in oxygen internal coordinates [6]. A phase diagram for the Hf-O system as a function of temperature summarizes these transformations in Figure 1.2.

Hafnium oxide also exhibits phase transformations induced by high pressure. Monoclinic HfO_2 undergoes a phase transition at 12 ± 0.5 GPa to a denser structure, orthorhombic I which belongs to space group $Pbca$ (Fig. 1.1d) [2, 10]. In the orthorhombic I phase the primitive cell doubles, however the coordination numbers for hafnium and oxygen remain unchanged [9]. A further increase in pressure to 28 ± 0.2 GPa transforms the orthorhombic I phase to a more stabilized polymorph, orthorhombic II; if the samples are taken to sufficiently high pressure, the orthorhombic II phase can be retained at room temperature [10]. The orthorhombic II phase belongs to space group $Pnma$ and has a higher coordination number, with the same units of HfO_2

in the primitive cell as the monoclinic phase; the coordination number of Hf increases from 7 to 9 (recall the monoclinic phase which has a seven fold-coordination) [9,10]. The unit cell dimensions for the specific crystal structures are also noted on Figure 1.1.

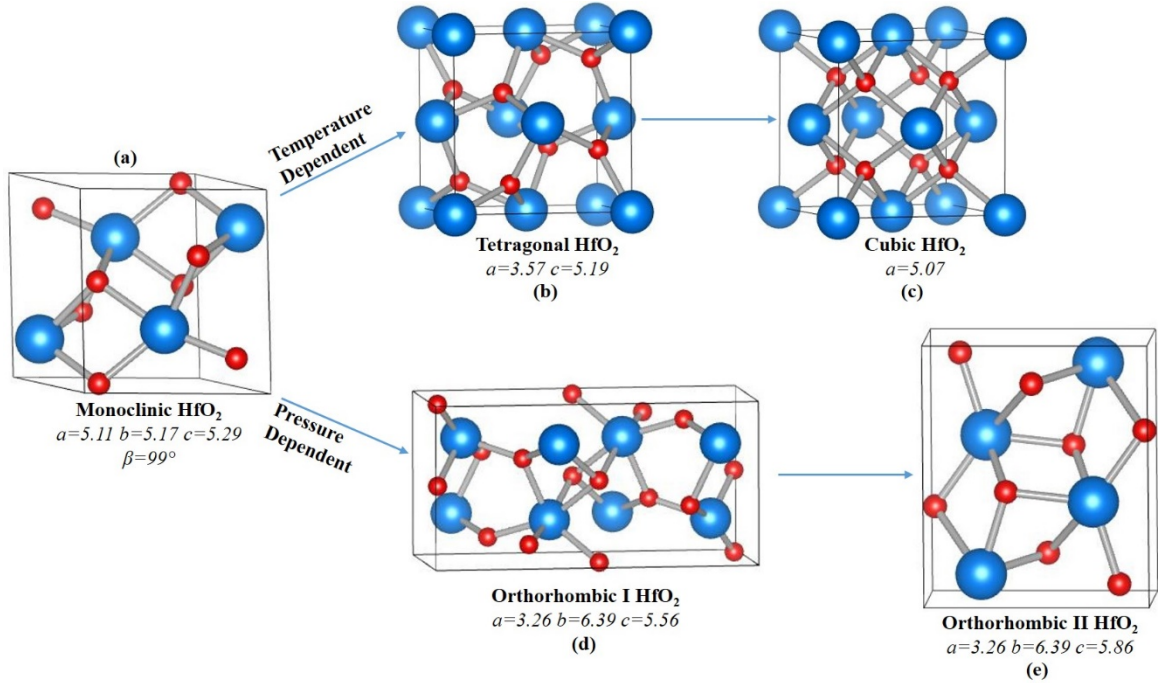


Figure 1.1 Unit cells of HfO_2 structures along with unit cell parameters [18] (a) monoclinic unit cell, P21/C; (b) tetragonal unit cell, P42/nmc; (c) cubic unit cell, Fm3m; (d) orthorhombic I unit cell, Pbca; (e) orthorhombic II unit cell, Pnma. (See [4])

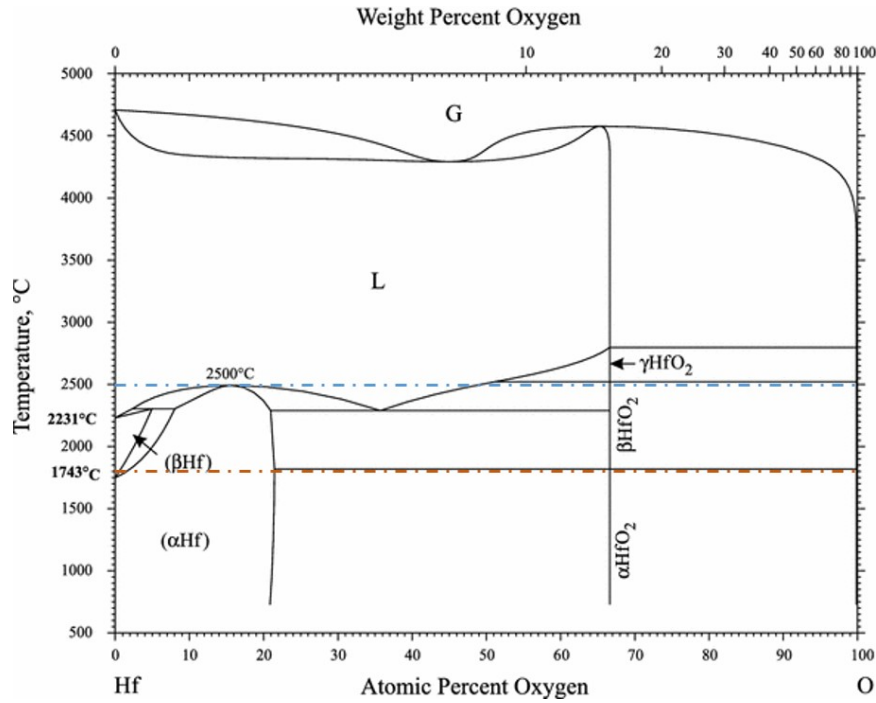


Figure 1.2 Phase diagram for the Hafnium-Oxygen system, indicating the proposed temperature dependent phases of HfO_2 [8].

1.2 Properties of HfO_2 Thin Films

Over the past few decades, HfO_2 has attracted much attention within the scientific research and technology development community due to its collection of diverse, attractive properties. Specifically, the structural, mechanical, optical and electrical properties of low dimensional HfO_2 structures have been receiving significant attention in recent years due to the possible options for tailoring the structure-property relationships at the reduced dimensions [3]. The focus is now directed at an overview of the significant properties of HfO_2 and the associated applications.

1.2.1 Optical Nature

The most essential optical properties of a thin film are based upon the dielectric properties, mainly the refractive index (n) and the extinction coefficient (k). HfO_2 is known for its relatively high dielectric constant ($k=25$) as well as a high index of refraction ($n\sim 2$) and as a result, HfO_2 is employed in optical coating applications, including filters, beam splitters, anti-reflection coatings and high-reflectivity mirrors [9,11]. HfO_2 has a wide transparency range extending down to 220 nm in the deep ultraviolet (DUV) range to 10 μm in the infrared (IR) spectral region [11]. For this reason HfO_2 is frequently used as a high-index, tough material when high laser damage threshold is a requirement.

In optical and optoelectronic coatings, it is always advantageous to use the highest and lowest indices available for all dielectric coatings in the spectral region of interest for device design and engineering [12]. UV transparent materials are important in the design and fabrication of high-quality and high-reflectivity multilayer coatings. Significant properties to consider a thin film high quality are low absorption in the wavelength region of interest, smooth interfaces with low levels of scattering, high laser damage threshold, and film densities approaching those of bulk materials [13]. There is a scarcity of high-index materials in the UV because there is higher absorption at wavelengths near the electronic bandgap [13]. The number of UV transparent materials is limited, in addition there are only a few suitable high-low refracting combinations [13]. Possible material contenders include metal oxides (Al_2O_3 , Y_2O_3 , Sc_2O_3 , ZrO_2 , and HfO_2) and wide bandgap fluorides (LaF_3 , NdF_3 , GdF_3) as high refractive index materials, and SiO_2 and other fluorides (MgF_2 , Na_3AlF_6 , AlF_3) as low refractive index materials [13]. Combinations that include oxides benefit from higher mechanical stability. Among metal

oxides that meet this criteria, HfO_2 and SiO_2 are the most important for the manufacture of UV transparent materials.

A typical multilayer structure consists of three-layer coatings of dielectric/metal/dielectric (D/M/D) on glass substrates and serve as spectrally selective coatings for various purposes [14]. The materials selection and thickness of the three layers influence the optical properties of the D/M/D system and can be tailored to suit different applications [14]. HfO_2 has relatively low levels of losses down to 230 nm and hence can be employed as high refractive index material for fabrication of high-reflectivity mirrors at 300- and 250- nanometer wavelength regions. Similarly, the solar spectrum is roughly split between the visible (wavelength from 400 to 700 nm) and the near-infrared (wavelength from 700 to 2000 nm) regions; for warm climates it would be desirable to design energy-efficient windows that reflect the infrared part of the solar spectrum, while transmitting visible light. When used to transmit visible light and reflect the infrared part of the solar spectrum, the D/M/D structure on glass is called a heat mirror. The metal layer is essential to reflect the infrared radiation; this layer transmits very little energy in the visible, and is therefore sandwiched between the two dielectric layers that act as antireflective coatings to enhance the energy transmitted in the visible region [14]. HfO_2 was proposed to be the desirable dielectric for the aforementioned heat mirror applications due its optical and structural properties [14]. HfO_2 films met the transparency requirement over the entire solar spectrum. Moreover the films were highly dense, obtaining a relative density of 0.85, along with a high refractive index [14]. The mechanical, thermal and chemical stability make HfO_2 heat mirrors durable and environmentally stable, with minimal interfacial reactions.

1.2.2 CMOS Technology and Electronic Properties

The silicon-based microelectronics industry steadily advanced the integrated circuit technology in accordance with Moore's famous law to meet the continuously raising demands regarding size, power consumption, and many other characteristics of state-of-the art complementary metal-oxide-semiconductor (CMOS) technology [17]. For the last 30 years SiO₂ has been the most common material for gate oxides, and with vast improvements in processing it is feasible to produce high-quality SiO₂ layers with the required thickness and very few electronic defects in amorphous structures as well as ideal interfaces with Si [17,18]. However, the problem remains in the fundamental thickness limitation for SiO₂ gate oxide layers of ~1.2. To further explain, the tunneling current-density (j) is considered:

$$\frac{\rho_m(E_t)}{V} \{f_m(E_t)[1-f_i(E_t)]-f_i(E_t)[1-f_m(E_t)]\} \frac{8\pi\hbar l}{E_t} (\int dS \cdot j_{if})^2 \cdot A/\text{cm}^2 \quad (1)$$

where $\rho_m(E_t)$ is the number of allowed quantum states on the equal-energy surface in the reciprocal space of the electrode, V , \hbar , l , $f_m(E_t)$, are the volume of the electrode, the reduced Planck's constant, the thickness of the electrode, and the Fermi-Dirac distribution of electrons designating the occupancy of an energy state of E_t in the electrode and insulator, respectively [18]. For SiO₂ gate oxide layers of 1.2 nm, this means that the electron tunneling results in a leakage current level that is unacceptably high even for high performance devices, and much too high for increasingly popular low-power applications [18,19].

The aggressive demands for the scaling down of silicon CMOS transistors has made it necessary to replace the SiO₂ gate oxide with an alternative, high dielectric constant oxide. The proposed material with a higher dielectric will allow to use a physically thicker layer of the oxide

but with the same capacitance per unit area; more commonly known as the equivalent oxide thickness (EOT),

$$\text{EOT} = d_{\text{H,K}} \cdot K_{\text{SiO}_2} / K_{\text{H,K}} \quad (2)$$

where $d_{\text{H,K}}$ is the thickness of the high dielectric oxide, and K is the dielectric constant [20]. A promising alternative high- K material should have a dielectric constant between 10 and 30, a bandgap above 5 eV, higher permittivity, a high quality interface with Si, and few interface defects or defect states within the Si band gap [18-20]. However, there is a contraindication when looking at the variation of dielectric constant with band gap of high- K oxides as seen in Fig. 1.3. Another important factor to consider is the thermodynamic stability of oxides in contact with Si; stability requires that the reactions of oxide with the metal be endothermic to avoid SiO_2 and metal silicide formation [20]. The choice of oxides then becomes limited to materials such as MgO , SrO , and CaO , or HfO_2 , ZrO_2 , Al_2O_3 , Y_2O_3 , or La_2O_3 . Further limitation, excludes group IIA oxides such as CaO because they are too reactive, and there is not sufficient data proving the stability of ZrO_2 in contact with Si. Therefore the main contenders remain HfO_2 , Y_2O_3 , Al_2O_3 , and La_2O_3 (along with their compounds) [20].

Hafnium oxide remains to be the highly qualified candidate although several oxide materials have been investigated for their potential as a gate dielectric in CMOS devices. HfO_2 has a high permittivity, relatively wide bandgap at ~ 5.7 eV, and along with a high- K it can be scaled down to ideal EOT's [20]. Other characteristics that make HfO_2 the leading contender are a larger heat of formation than SiO_2 (-1300 kJ/mol versus SiO_2 at -1050 kJ/mol), good thermal and chemical stability with silicon, and adequate compatibility with n^+ polysilicon gate electrodes [18-20]. At an operating voltage of 1-1.5 V, the leakage current through HfO_2 dielectric films was reported to be several orders of magnitude lower than that of SiO_2 with the

same EOT, 0.9-2 nm, also in consequence of reasonably high barrier height that limits electron tunneling [18]. A disadvantage for HfO_2 is that a crystallization temperature is easily achieved, however this does not pose a threat to the leakage current at low field, hence the scalability still outweighs [20]. Further improvement of properties however, remains for HfO_2 concerning its interface with silicon. Choi et al. emphasizes the need to understand HfO_2 and other Hf-based materials and their interfaces for the success of CMOS technology since the chemical potential difference and reaction kinetics dictate the resulting electronic properties and may be dramatically improved by altering the chemical environment at the interfacial [18]. Figure 1.4 (a) and (b) focus on the effect of band alignment of Hf-based materials with silicon, one of the requirements for CMOS devices. The interface of HfO_2 with various semiconductors is illustrated by various band diagrams ultimately demonstrating potential applications into silicon based devices with a high mobility channel or non-silicon based devices.

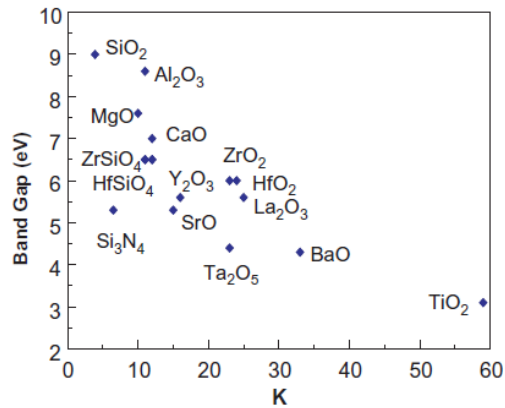


Figure 1.3 Variation of dielectric constant with band gap [20]. The choice for high- K materials becomes limited since there is a contraindication with band gap selection.

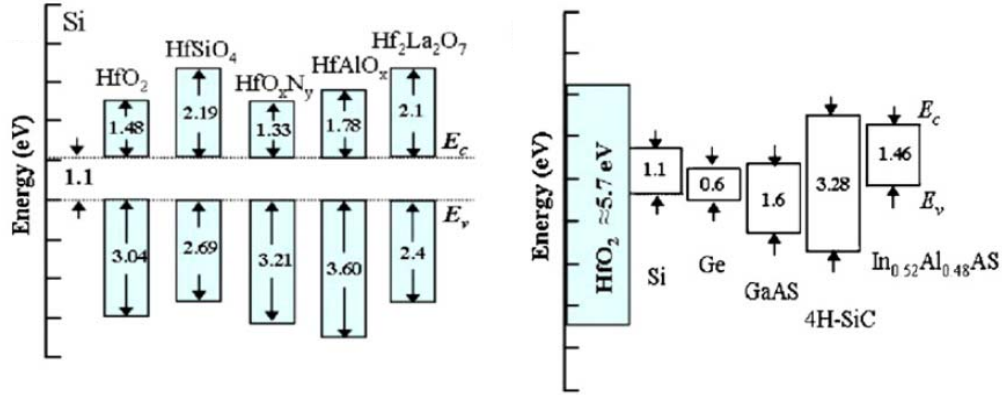


Figure 1.4 (a) Band diagrams of hafnium-based materials on Si and (b) band diagrams of HfO₂ on different semiconductors for potential applications into Si advance technologies as well as non-silicon based devices [18].

Another distinct phenomena of HfO₂ that has created some controversy in the scientific community, is the idea of ferromagnetism in this ‘traditionally known dielectric material.’ The ions of HfO₂ have homologous outer shell configurations, Hf⁴⁺[Xe]4f¹⁴ and O²⁻[Ne] [17,21,22]. According to the magnetism theory, HfO₂ should be nonmagnetic because of either full or empty d and f shells of the Hf⁴⁺ and O²⁻ ions [21]. Besides dopants such as Ni or Fe, the phenomena of ferromagnetism in undoped HfO₂ is discussed by Coey et al. whom attribute it to “d⁰ ferromagnetism” which may be a result of lattice defects located near the interface with the substrate [22]. If this characteristic is found to be true and exploited, it will undoubtedly expound HfO₂ for advances in the spintronics field. The combination of ferromagnetism with the good dielectric characteristics of HfO₂ films should enable the integration of CMOS with spintronic technology [17,21]. This will also enhance the understanding of the underlying mechanism of diluted magnetic semiconductor (DMS) behavior which has been actively researched in recent years [21].

1.2.3 Mechanical Behavior

Stabilized HfO₂ is resistant to oxidation but is particularly susceptible to oxygen diffusion, through oxygen vacancies in the lattice, as is reported in many defect structures of HfO₂ [23,24]. Moreover, HfO₂ is not easily attacked by most chemical reagents at room temperature making it a good material for corrosion protection. HfO₂ is a good candidate for hard materials with a high melting point (~2800 °C) which makes it suitable for high temperature structural ceramics applications including, engines, hypersonic vehicles, plasma arc electrodes, cutting tools, furnace elements, and high temperature shielding [23]. HfO₂ is moderately incompressible with a bulk modulus of 145 GPa. The reported values on bulk moduli for HfO₂ dense structures ranges from 212 GPa for monoclinic HfO₂, 243 GPa for orthorhombic I and up to 400 GPa for the orthorhombic II phase [1,23]. The more common structural and mechanical properties of HfO₂ are summarized in Table 1.1.

<u>Physical/Chemical Property</u>	<u>Magnitude</u>
Density	9.68 g/cm ³
Melting Point	2812 °C
Thermal Conductivity	1.67 (W/m·°C)
Thermal Expansion	6.5(10 ⁻⁶ /°C)
Electrical Resistivity	109 Ω·cm
Vickers Hardness	14.71 GPa
Flexural Strength	110 MPa
Compressive Strength	1380 MPa

Table 1.1. Summarized characteristics and mechanical properties of bulk HfO₂ [24].

1.3 Fabrication Techniques

Recall the importance of the thickness of high-*K* HfO₂, which is on the orders of nanometers; thin film processing parameters and process chemistry are critical factors of film

homogeneity and dielectric performance, signifying the importance of chemical processing and its control [18]. HfO_2 can be fabricated by various techniques such as chemical vapor deposition, electrochemical deposition, atomic layer deposition, pulse laser deposition, radio frequency (RF) and direct current (DC) magnetron sputtering. The individual methodologies manipulate the resulting properties such as growth rate, and in turn have their own merits and demerits as summarized in Fig. 1.5 [18]. Some of the disadvantageous that CVD methods pose is the risk of incorporating impurities due to the metal-organic or halogen containing precursors. Although, atomic layer deposition also uses precursors it has the unique capability of forming porous structures from the highly dense HfO_2 structures which in turn can be used for gas sensing technologies. Ultimately, the more common fabrication method to form HfO_2 films is magnetron sputtering, a physical vapor deposition technique. It is a prominent method due to its simplicity, low contamination, and feasible reproduction for large scale operation [18]. The reactive sputtering process also provide other advantages like uniform coatings, good adhesion, and high deposition rates [25]. For the proposed work, RF magnetron sputtering was the method of choice, and will be explained further in the eventual chapters on the basis of processing.

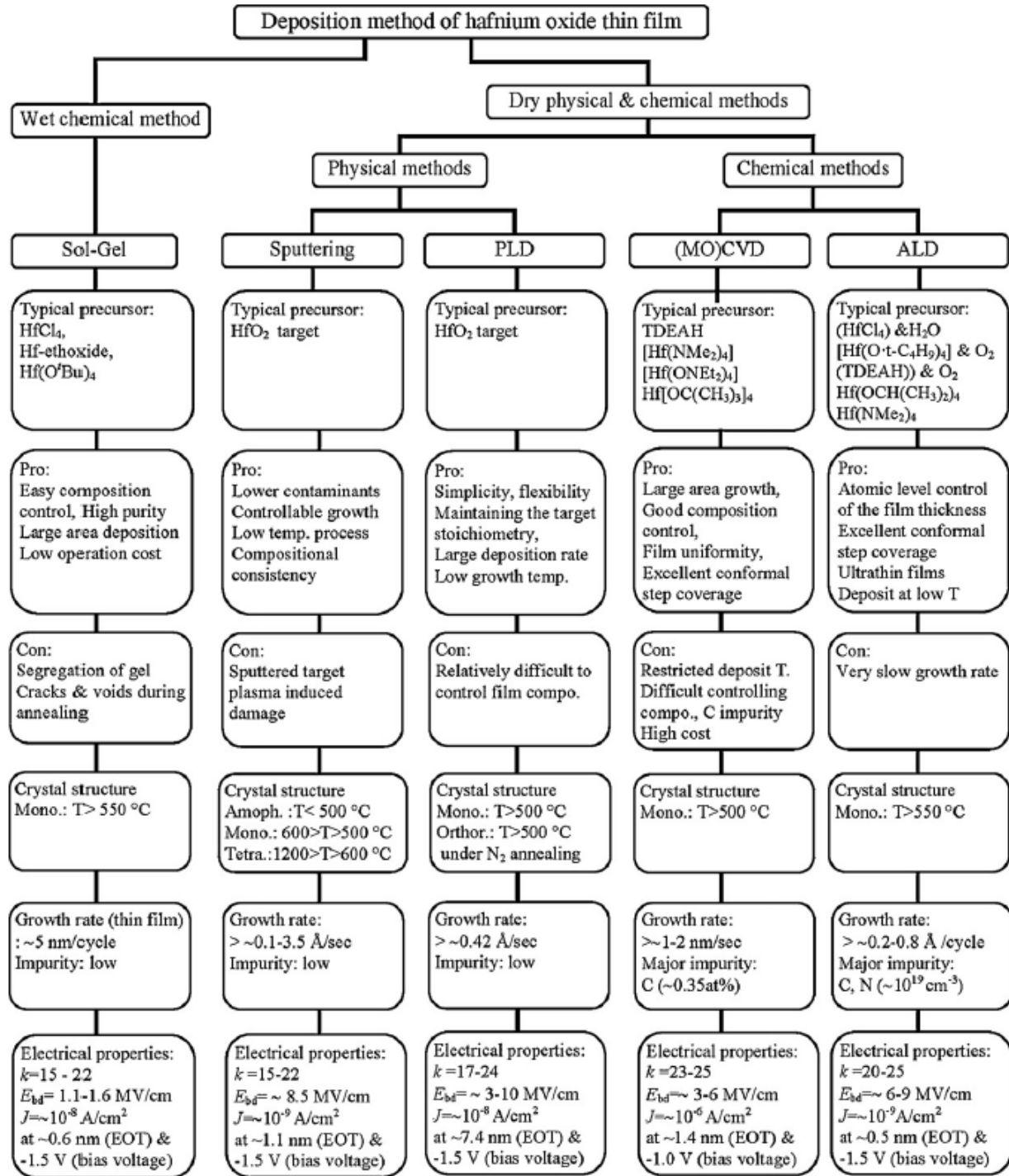


Figure 1.5 Deposition technique flow chart for HfO₂ depicting the pros and cons of typical fabrication methods [18].

Chapter 2: Literature Review

2.1 Literature Review

It is well known that HfO_2 is one of the most important high index materials for the production of optical multilayer coatings as well as electronic devices for CMOS technology. The understanding of the optical and electronic properties of HfO_2 stems from various factors. Structural defects or trap centers in HfO_2 can highly affect the resulting properties, which are also highly dependent on the structural characteristics such as structure, crystallite size, crystallographic texture and morphology, and chemistry. From the viewpoint described above, it is necessary to look into the effect of processing conditions and parameters on the observed properties of HfO_2 films.

HfO_2 films are usually fabricated at low enough temperatures or ambient conditions, that the monoclinic phase is more prone for crystallization, and in addition to being the most thermodynamically stable phase, it is highly desired for opto-electronic applications. Ma *et al.* [26] reported on the observed crystallization of HfO_2 films grown at various conditions through RF magnetron sputtering. The films were polycrystalline and due to the texturing orientation they were ambiguously assigned to monoclinic HfO_2 . The $(\bar{1}11)$ orientation in monoclinic HfO_2 will primarily populate since it has the lowest surface free energy in this phase and is expected around 28° on a 2θ scale [26]. Crystalline parameters such as grain size and d-spacing were measured through the Scherrer equation and x-ray diffraction patterns. The relationships confirmed were an increase in grain size with increasing growth temperature, and a decrease in d-spacing with a limit on temperature conditions, and afterwards the lattice expanded. This is because for small crystallites, the lattice expansion in ionic solids can be attributed to causes such as a reduction in cation charge state and repulsion of strong surface dipoles leading to a

reduction in surface tension (Hf forms cations with only a single charge state of +2; surface dipole repulsion causes the lattice expansion in small crystallites) [26]. However, upon reaching a peak in growth temperature the main reason for the expansion in the larger crystallites could be the strain induced in the $(\bar{1}11)$ preferred orientation. Recently, Szymanska *et al.* [27] also looked at the effect of reactive magnetron sputtering parameters (among them: pressure in the reactor chamber, Ar and O₂ flow rates, power applied to the reactor chamber and deposition time) on structural and electrical properties of HfO_x films. An amorphous behavior for the films was observed at room temperature, and a deterioration of the homogeneity in the film was evident after high temperature treatment. The increase in crystal nature of the films is correlated to the observed undesirable deterioration of electro-physical properties when the films were grown for gate dielectrics in a metal-insulator-semiconductor structure [27].

Maidul Haque *et al.* [28] fabricated HfO₂ samples through RF magnetron sputtering, and varied oxygen-partial pressure; microstructural, optical and physical properties were evaluated. Film growth behavior was also investigated by applying a DC bias on the substrate. GIXRD measurements suggested that all the samples exhibited the monoclinic phase, and there was no significant change in the crystallinity of the samples due to substrate biasing. Through Rutherford backscattering measurements, the atomic densities of the films were calculated; the atomic densities of the films deposited without oxygen partial pressure were higher than films deposited with 9.1% oxygen partial pressure. Optical measurements dictate the refractive indices of the films deposited without oxygen high and then decreased for both set of films (with and without substrate biasing) when deposited with 9.1% oxygen partial pressure. In general applying a substrate bias will yield higher values for the index of refraction. It was also observed that with an increase in oxygen partial pressure, the refractive index shows an increasing trend

for films deposited without substrate bias. Band gap measurements were low for films deposited without additional oxygen, and developed higher values when deposited at oxygen partial pressures of 15% and greater. Maidul Haque *et al.* [28] were able to develop a correlation between film properties and oxygen partial pressures due to the following: as oxygen partial pressure was increased during deposition, bombardment of the growing films by negative oxygen ions in the positive half cycle of the bias was increased leading to oxygen rich low density films. Therefore, the films deposited without any substrate bias and oxygen partial pressure >15% show an increasing trend in density values, while for the other set deposited with substrate bias, density of the films did not increase rather decreased slightly [28].

HfO₂ films and coatings have become the preferred material for optical components. Al-Kuhaili [14] successfully proposed HfO₂ films ideal for optical heat mirrors by depositing a D/M/D structure as HfO₂/Ag/HfO₂ and investigating suitable properties specifically optical behavior. For the three layer system the HfO₂ thin films were deposited by electron beam evaporation, and the silver layer was evaporated from a tungsten boat. The films were amorphous, homogeneous and transparent down to a wavelength of 300 nm. A theoretical model was developed to further study and optimize the D/M/D structure, by applying detailed numerical calculations to find out the optimum set of parameters for the operation of the heat mirror. The results concluded that the dielectric layers should have the same thickness with a high refractive index. The metal layer should have high transparency in the visible region, and the thickness should be minimized to avoid a decrease in transmittance. The HfO₂ based heat mirror showed ideal transmittance in the visible region (72.4% for $\lambda=400-700$ nm) and the average reflectance in the near infrared region was 67% for $\lambda=700-2000$ nm. Khoshman *et al.* [29] have also proposed amorphous HfO₂ films as good candidates for antireflection optical

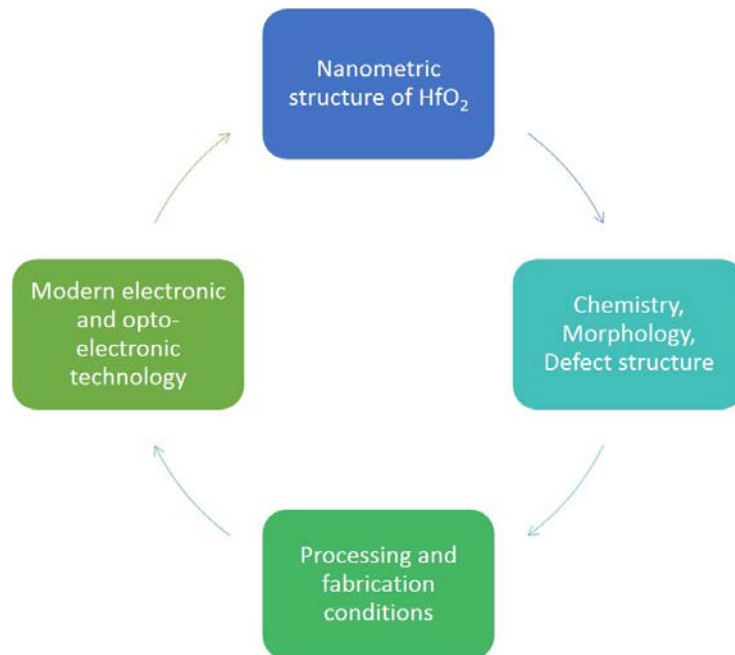
coatings, and in doing so they also studied the effects of annealing temperatures on the structure and optical properties of the amorphous films. The films were fabricated through RF magnetron sputtering at temperatures $<52\text{ }^{\circ}\text{C}$ and annealed the films using a rapid thermal anneal (RTA) at $1000\text{ }^{\circ}\text{C}$ for 1.5 h in a pure Ar ambient at atmospheric pressure. The spectral dependence of the reflectivity of the as-deposited was considerably lower ($<8\%$) than the monoclinic crystalline structure ($<16\%$) within the wavelength range 200-850 nm at normal incidence. The amorphous sample was concluded to have a higher transmissivity as well.

Band gap values increased from 5.68 eV for the as-deposited to 5.99 eV for the annealed films. The increase in band energy after annealing is due to the crystallization of HfO_2 . The difference of 0.35 eV between the two phases is attributed to the fact that the structure of amorphous solids is characterized as an irregular arrangement of atoms. This disorder is known to influence the optical band ‘gap’ of amorphous semiconductors as well. Khoshman *et al.* [29] observed an additional absorption peak, indicating the existence of additional energy states at about 0.4 eV as a result of trap levels. The trap levels are due to the existence of the amorphous phases within the crystallized HfO_2 film after annealing [29]. Cisneros-Morales *et al.* [30] consequently reported that electronic states close in energy to the fundamental optical absorption edge form intragap charge trap states; a feature at a slightly higher energy than O defect states was observed as a broad low energy shoulder. Literature argues whether this feature is associated with defect states or intrinsic to the sevenfold Hf-O coordination in monoclinic HfO_2 . Cisneros-Morales *et al.* [30] have investigated the relationship between crystallite size, lattice expansion, and optical behavior of HfO_2 films deposited by sputtering and annealed post-deposition. Results achieved a band that initiated at 5.65 eV and saturated at 5.94 eV and appeared as a low energy shoulder, but developed into a discrete and more intense feature upon

continued annealing. Ultimately, the band's spectral position was unaffected by decreasing crystallite size and lattice expansion. However, the intensity of the band increased with increasing crystallite size, even after the lattice expansion reached a plateau.

2.2 Motivation

The possibility to tailor essential properties for transparent oxides such as HfO_2 allows for engineering modern electronic and opto-electronic devices. The nanometric structure or crystalline behavior, if any, decides the ideal device application based on the chemistry, morphology, and defect structure that make-up the thin film. These factors however are highly influenced by the method of fabrication, the processing parameters, and growth variables. The impetus for the present work is to derive a structure-property relationship in HfO_2 nanocrystalline films by exploring the changes in structural, physical, and optical properties as a function of variable growth temperature.



Chapter 3: Experimental Details

3.1 Film Fabrication

The HfO₂ films for this investigation were fabricated through RF magnetron sputtering, a physical vapor deposition technique. Physical vapor techniques rely on excitation of a source or target material that is usually solid to produce the necessary material for film formation [38-39]. During the sputtering process atoms are dislodged from a solid target through the impact of energetic gaseous ions [38-39]. The ionizing gas is usually high purity argon (Ar). Substrate material is placed opposite the target material in a vacuum chamber which is pumped to relatively low pressures. Applying a negative charge to the target material causes a plasma discharge. The positively charged gas ions become attracted to the negatively biased target surface, creating high speed collisions that will induce a momentum transfer and eject target atoms. The sputtered atoms have kinetic energies much greater than thermal energy and proceed in the direction of the substrate. The substrate is placed in front of the target so that it can intercept the flux of sputtered atoms. In RF magnetron sputtering, a RF power source is used (13.56 MHz is a commercial frequency often used). The electrons discharged from the target material do not contribute significantly to sustaining the ejected atoms onto the substrate surface and are likely to cause unwanted heating, however if a magnetic field is applied parallel to the target surface, the secondary electrons circle around the magnetic field lines and stay near the target, ultimately increasing ionization efficiency [38-39]. Figure 3.1 depicts the principle of RF magnetron sputtering. RF magnetron sputtering is ideal for the deposition of insulators as well as achieving improved morphology, microstructure, and interfaces [28]. Figure 3.2 is the sputtering system used for the HfO₂ films in this work.

The methodology for film deposition in this investigation is as follows: HfO₂ films were deposited onto silicon (100) wafers and quartz substrates by radio frequency magnetron sputtering. All the substrates were thoroughly cleaned and dried with nitrogen before introducing them into the vacuum chamber, which was initially evacuated to a base pressure of $\sim 10^{-6}$ Torr. A hafnium (Hf) target (Plasmaterials, Inc.) of 2 in. diameter and 99.95% purity was employed for sputtering. The Hf target was placed on a 2 in. sputter gun, which is placed at a distance of 8 cm. from the substrate. The sputtering gas was high-purity argon (Ar), while oxygen (O₂) was introduced during deposition for reactive growth to form Hf-oxide. A power of 100 W was employed for reactive deposition. The ratio of Ar to O₂ was kept at 70:30 (28 sccm Ar mixed with 12 sccm of O₂), and the respective flow of each gas was monitored using an MKS mass flow meter. Before each deposition, the Hf target was pre-sputtered for 10 min with a shutter above the gun closed. The deposition time was carried out for 45 minutes. The thicknesses of the crystalline films were in the range ~ 30 -60 nm. Growth temperature (T_s) was varied in the range of room temperature ($RT=25^\circ\text{C}$) to 700°C . The other variables such as sputtering power, pressure, and flow of Ar and O₂ and their ratio were kept constant.

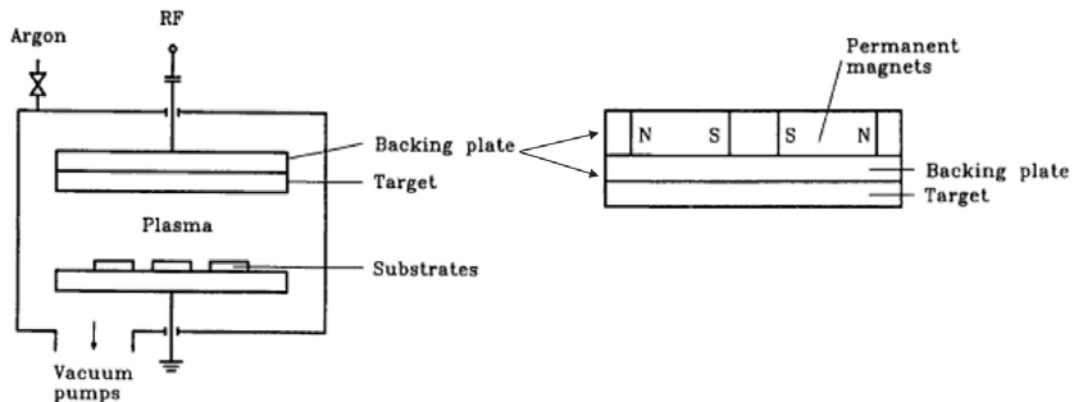


Figure 3.1 Principle of an rf sputtering system, demonstrating the role of the magnetic field [39].

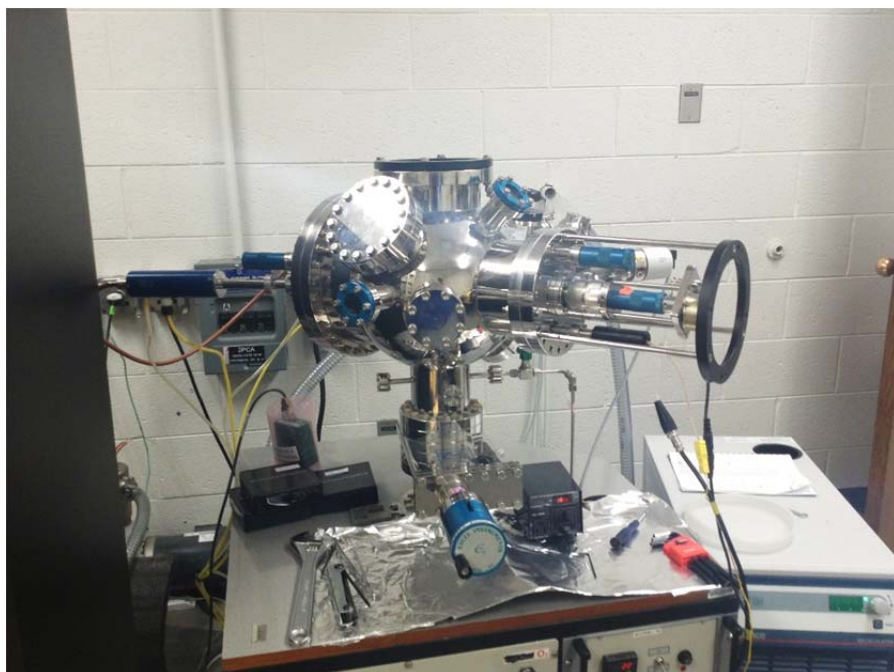


Figure 3.2 Sputtering system employed for the growth of the HfO_2 films.

3.2 Film Characterization

The grown HfO_2 films were characterized by performing non-destructive techniques for crystal structure, surface morphology, and optical measurements.

3.2.1 *X-Ray Diffraction (XRD)*

X-ray diffraction (XRD) techniques rely on the characteristic wavelength of a particular X-ray source and the response after interacting with a crystalline or amorphous material. Upon the interaction of an incident beam of monochromatic X-rays with a crystal, the beam will diffract into many specific directions related to the crystal. The scattered X-ray will undergo constructive or destructive interferences based on crystalline or amorphous behavior. Bragg's law must be satisfied in order to obtain valuable information such as phase identification, unit cell dimensions, or a measurement of purity. X-rays are generated in a cathode ray tube by

heating a filament to produce electrons, and applying a voltage to accelerate the electrons to a sample material. Once the electrons have generated sufficient energy to dislodge inner shell electrons of the sample material, a characteristic X-ray spectra is produced. For thin film analysis it is formal to use grazing incidence XRD or GIXRD, in which the X-ray beam will only penetrate the sample surface at very small angles of incidence, and avoid a substrate diffractogram.

XRD measurements on HfO₂ films grown on Si were performed using a Bruker D8 Advance X-ray diffractometer (Fig. 3.3). All the measurements were made ex situ as a function of growth temperature. In order to avoid interference by the substrate and obtain diffraction pattern of the coatings, grazing incidence X-ray diffraction (GIXRD) were performed on the films. XRD patterns were recorded using CuK α radiation ($\lambda = 1.54056 \text{ \AA}$) at room temperature. High resolution scans were also performed on evident crystallization peaks with parameter of a step size of 0.01 degree per 1 s. The crystalline domain size was calculated through the use of the Scherrer relationship, after removal of background artifacts. The Scherrer equation is defined by,

$$D_{hkl} = 0.9\lambda / \beta \cos \theta \quad (3)$$

where D_{hkl} is the crystallite size, λ is the wavelength of the filament used in the XRD machine, β is the full width half maximum of the peak corrected for instrumental broadening, and θ is the angle of the peak [40,41]. Bragg's law was used to calculate the interplanar spacing $d_{(hkl)}$, from 2θ .

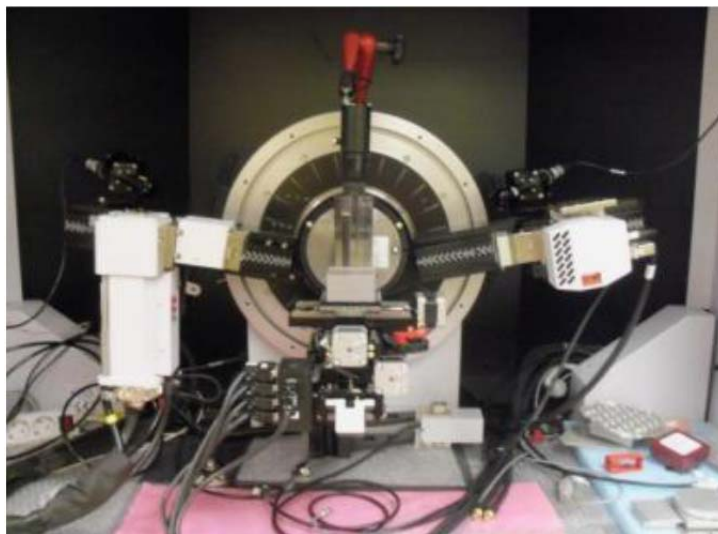


Figure 3.3 Bruker D8 advanced diffractometer used for GIXRD scans.

3.2.2 *Scanning Electron Microscopy (SEM)*

Electron microscopy utilizes a beam of high energy electrons generated from a suitable source, in the present case a field emission gun. The electron beam is accelerated through a high voltage and will go through a series of electromagnetic lenses, deflection coils, and stigmators that will control and refine the electron beam after it leaves the electron gun, and before it strikes the specimen. The high kinetic energy that the electrons carry will dissipate as a variety of signals as the beam interacts with the specimen material, of which the more important ones include secondary and backscattered electrons which produce SEM images. The secondary electrons are essential for the morphology and topography of the specimen and backscattered electrons illustrate contrasts in material composition. Imaging is produced when the electron beam is scanned from top to bottom left to right, or a raster pattern. The emitted electrons are detected for each position in the scanned area by an electron detector [42].

Surface imaging analysis was performed using a field emission scanning electron microscope (Hitachi S-4800) (Fig. 3.4). Secondary electron imaging was performed on HfO_2 films grown on Si wafers using carbon paste at the ends to avoid charging problems.



Figure 3.4 Hitachi S4800 SEM.

3.2.3 Atomic Force Microscopy (AFM)

Atomic force microscopy is a type of scanning probe microscopy technique which is used to image surface structures on the nano to subnano scale. A microscopic tip attached to a cantilever spring is scanned across the specimen surface to obtain information such as topography, or measurements of the material's physical, magnetic, and chemical properties. The probe is also scanned in a raster pattern to form a map of the measured property relative to the X-Y position. An AFM image will then depict the variation in the measured property such as height or magnetic domains across the scanned area. The probe is attached to a piezoelectric scanner tube, which scans the probe across a selected area of the sample surface [42].

Interatomic forces between the probe tip and the sample surface cause the cantilever to deflect as the sample's surface topography (or other properties) changes [42]. A laser light reflected from the back of the cantilever measures the deflection of the cantilever [42]. This information is fed back to a computer, which generates a map of topography and/or other properties of interest; areas as large as about 100 μm square to less than 100 nm square can be imaged [42]. Figure 3.5 is a schematic representation of an AFM instrument configuration.

Surface morphology of the HfO_2 films was also studied by employing AFM using a Veeco Multimode scanning probe microscope with a Nanoscope V controller. AFM images were acquired using the ScanAsyst mode which utilizes a Bruker proprietary method for curve collection and sophisticated algorithms to continuously monitor image quality, and automatically make appropriate parameter adjustments [43]. Aluminum coated silicon cantilevers (Bruker, USA) were used to acquire ScanAsyst mode images. The cantilevers measure 115 μm long, 25 μm wide and 0.65 μm thick with a spring constant of 0.4 N/m a resonance frequency of 70 kHz. Tip quality was qualitatively assessed by the clarity and presence of artifacts in the acquired images. The calibration standard used to calibrate the scanner consisted of platinum-coated, 200 nm-tall silicon columns spaced at 10 μm intervals on centers. The columns have a length of 5 nm on a side.

AFM images (512 scan lines & 512 pixels per scan line) were acquired with an integral gain of approximately 2, a proportional gain of approximately 50, and an amplitude setpoint of 200 mV. The drive amplitude varied between 30 and 180 mV. The images were then subjected to a 3rd order flattening procedure using the Veeco Nanoscope software to remove the non-linear background artifact introduced by the piezo scanner. Following the flattening procedure, the surface roughness was quantified using the aforementioned software.

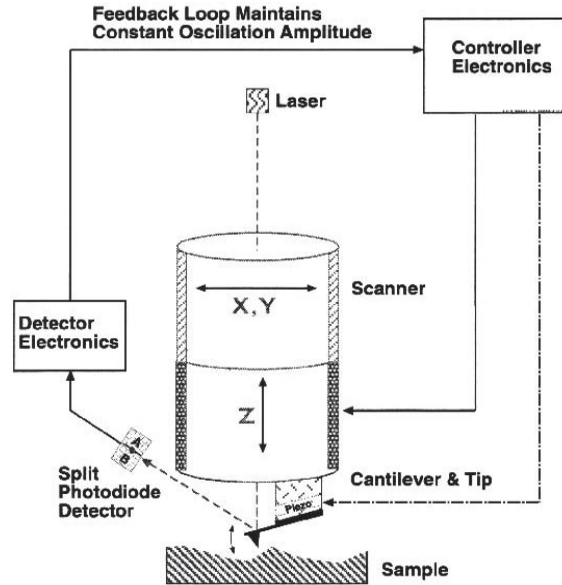


Figure 3.5 Schematic representation of an AFM instrument configuration [42].

3.2.4 X-Ray Reflectivity (XRR)

X-ray reflectometry (XRR) is used to analyze X-ray *reflection* intensity curves as opposed to XRD that relies on *diffraction* phenomena. Information is gathered from a grazing incident X-ray beam to determine film properties such as thickness, density, and surface or interface roughness. XRR may be used to evaluate single-crystalline, polycrystalline, or amorphous materials. When electromagnetic waves including visible wavelength are incident upon a sample surface, they will reflect off. The incident electromagnetic waves generate a specularly reflected wave, a refracted wave and diffused reflections, as shown in Figure 3.6. X-rays which are incident electromagnetic waves undergo a total reflection when incident on a flat surface of a material at a grazing angle smaller than the critical angle for total reflection (θ_c) as is the case in Figure 3.7 [44].

XRR is best effective when the layer material has different electron densities per layer. Interference occurs between X-rays reflected from a film surface and the interface between film

and substrate. The reflectivity profile will show oscillations caused by this interference (called Kiessing fringes); and the oscillations are dependent upon film thickness, and the thicker film the shorter the period of the oscillations [44]. The amplitude of the oscillations and the critical angle provide information on the density of the films. Surface and interface roughness will impact the decay of reflected X-rays. Figure 3.8 demonstrates the detail of information provided by XRR spectra. For density and roughness determinations, precision is about 5-10%, whereas it is less than 3% for the thickness [45].

XRR measurements were performed on a Rigaku Smartlab X-ray diffractometer (Fig. 3.9). A $\text{CuK}\alpha$ X-ray source is used by the Smartlab diffractometer. Scans were taken at a speed of 0.2° per minute and a step size of 0.005° . The total length of scans were taken at low angles from 0° to 6° . Experimental data was then fit with the software package GlobalFit associated with Rigaku Smartlab diffractometer.

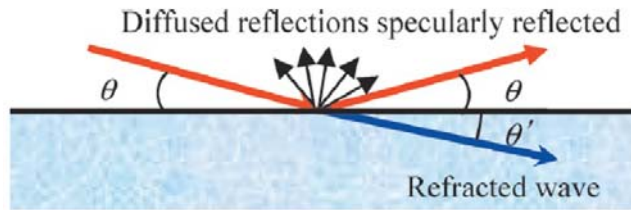


Figure 3.6 Reflection and refraction of X-rays on a material surface [44].

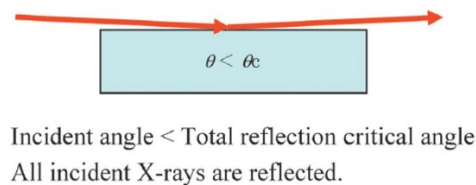


Figure 3.7 Schematic representation of X-ray incident beam when the incident angle is less than the critical angle [44].

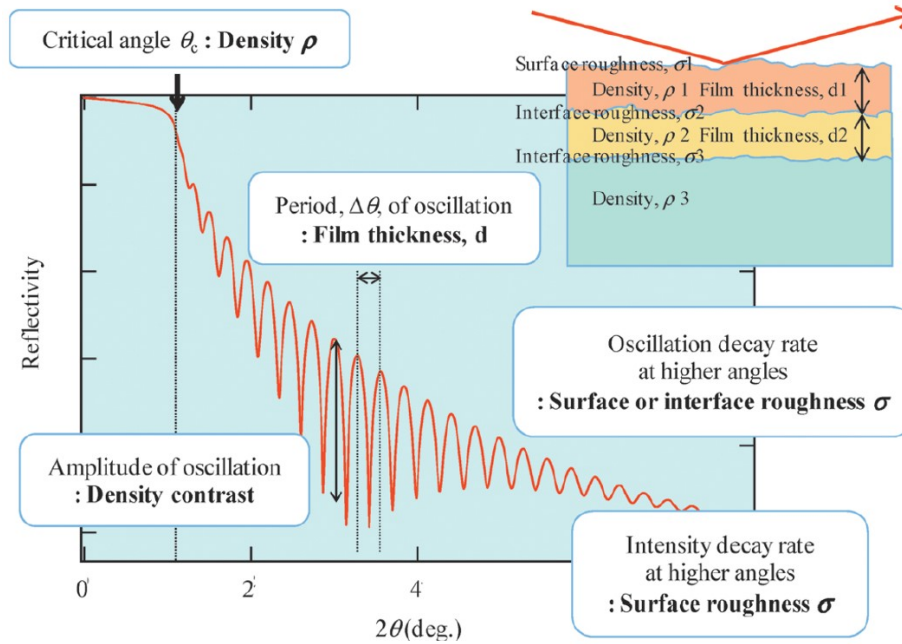


Figure 3.8 Structural information provided by X-ray reflectivity profile [44].

3.2.5 Spectrophotometry Measurements

Spectrophotometry measurements are employed to quantify the amount of light that a sample absorbs as a function of wavelength. If all light (UV to the visible spectrum) passes through the specimen without any absorbance the percent transmittance is 100%. Transmittance spectra is achievable through the Beer-Lambert law when light emerges propagating in the same direction as the incident light [46]. The experimental measurements are defined by:

$$T = I/I_0 \quad (4)$$

Where T is the transmittance, and I is the light intensity after it is emitted through the specimen, and I_0 is the initial light intensity [46].

Optical properties were evaluated using both spectrophotometric and ellipsometry measurements. Spectrophotometry measurements were attained by using a Cary 5000 UV-vis-

NR double-beam spectrophotometer (Fig. 3.9). Films grown on optical grade quartz were employed for optical property measurements to probe the transparent nature and band gap analysis of the HfO₂ films.



Figure 3.9 Cary 5000 spectrophotometer.

3.2.6 *Spectroscopic Ellipsometry (SE)*

Spectroscopic ellipsometry (SE) measures the relative changes in the amplitude and phase of the linearly polarized monochromatic incident light upon oblique reflection from the sample surface. The experimental parameters obtained by SE are the angles Ψ (azimuth) and Δ (phase change), which are related to the microstructure and optical properties, defined by:

$$\rho = R_p/R_s = \tan \Psi \exp (i\Delta) \quad (5)$$

where R_p and R_s are the complex reflection coefficients of the light polarized parallel and perpendicular to the plane of incidence, respectively [47-50]. In general, the fundamental equation of ellipsometry that relates the measurable with the accessible optical information is:

$$\rho = \tan \psi \exp (i\Delta) = \rho(N_0, N_1, N_2, L_1, \Phi_0, \lambda) \quad (6)$$

where the middle term contains the measurable and the last term on the right contains all the accessible parameters of the measurement, namely, film thicknesses, optical properties, the wavelength of light, and the angle of incidence [30]. The spectral dependencies of ellipsometric parameters Ψ (azimuth) and Δ (phase change) can be fitted with appropriate models to extract film thickness and the optical constants i.e., the refractive index (n) and extinction coefficient (k), based on the best fit between experimental and simulated spectra [47-50]. In the present case, the Levenberg-Marquardt regression algorithm was used for minimizing the mean-squared error (MSE):

$$MSE = \frac{1}{2N - M} \sum_{i=1}^n \left[\left\{ \frac{(\Psi_{\text{exp.}} - \Psi_{\text{calc.}})}{\sigma_{\Psi_i}^{\text{exp}}} \right\}^2 + \left\{ \frac{(\Delta_{\text{exp.}} - \Delta_{\text{calc.}})}{\sigma_{\Delta_i}^{\text{exp}}} \right\}^2 \right] \quad (7)$$

where $\Psi_{\text{exp.}}$, $\Psi_{\text{calc.}}$ and $\Delta_{\text{exp.}}$, $\Delta_{\text{calc.}}$ are the measured (experimental) and calculated ellipsometry functions, N is the number of measured Ψ , Δ pairs, M is the number of fitted parameters in the optical model and σ are standard deviations of the experimental data points [47].

In order to extract optimal data from SE experimental and simulated measurements, the construction of a multilayer optical model is essential. The model representation accounts for a number of distinct layers with individual optical dispersions and the interfaces between these layers are optical boundaries at which light is refracted and reflected according to the Fresnel relations. The dispersion relations of the optical constants are derived using a stack model; succeeding the construction of the optical layer model, the experimental data is fit with appropriate dispersion models. For the case of the HfO_2 thin films the data was fit with the conventional Cauchy dispersion model, because the films are transparent in the visible region the Cauchy model is optimal [51]. The Cauchy equation can be expressed approximately as a refractive index n as a function of wavelength λ :

$$n(\lambda) = a + b/\lambda^2 + c/\lambda^4 \quad (8)$$

where A, B, and C are the Cauchy coefficients and specific to the material, A is the constant that dominates $n(\lambda)$ for long wavelengths, B controls the curvature of $n(\lambda)$ in the middle of the visible spectrum, and C influences $n(\lambda)$ to a greater extent in shorter wavelengths [47-51]. Note that this principle behind Cauchy's polynomial is also used for the dispersion function $k(\lambda)$:

$$k(\lambda) = d + e/\lambda^2 + f/\lambda^4 \quad (9)$$

where d, e, and f are constants specific to the material [47-51].

SE measurements were performed ex-situ on the films grown on silicon wafers by utilizing a J. A. Woollam V-VASE instrument (Fig. 3.10). Measurements were done in the range of 300 to 1350 nm with a step size of 2 nm and at angles of incidence of 65°, 70°, and 75°, near the Brewster's angle of silicon. The ellipsometry data analysis was performed using commercially available WVASE32 software.

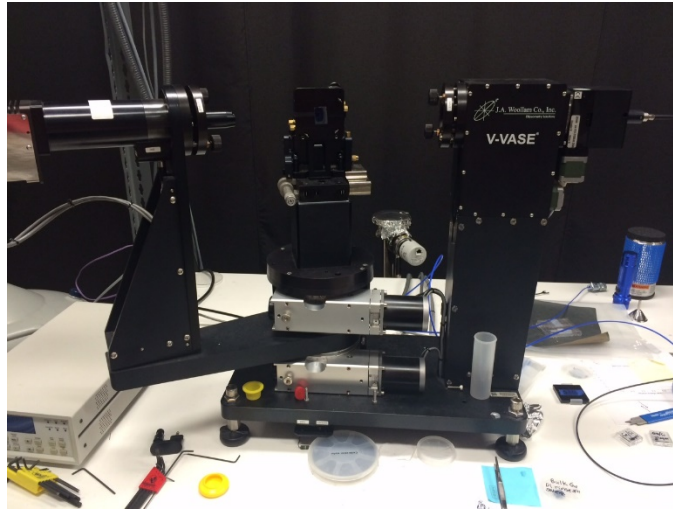


Figure 3.10 J.A. Woollam WVASE ellipsometer.

Chapter 4: Results & Discussion

4.1 Crystal Structure

X-ray diffraction patterns of HfO_2 films are shown in Figure 4.1a as a function of T_s . The patterns for films deposited at $T_s \geq 200$ °C exhibit crystalline nature oriented along the $(\bar{1}11)$, designating a crystallization temperature of 200 °C for monoclinic HfO_2 . The film remains amorphous for $T_s = \text{RT}$. However, the peak corresponding to $T_s = 200$ °C is minor and broad. The broad peak may be due to the presence of small crystallites within an amorphous matrix. The intensity of the $(\bar{1}11)$ peak increases with increasing growth temperature which indicates an increase in crystallite size with T_s . The films exhibit a strong $(\bar{1}11)$ texturing which is expected based on phase-stability considerations [3,52]. It is well-known that $(\bar{1}11)$ planes will primarily populate as they exhibit the lowest surface free energy, although minor peaks due to other orientations of monoclinic phase are also present at higher temperatures. High resolution scans of $(\bar{1}11)$ peaks are shown in Figure 4.1b. The high resolution scans were performed on $(\bar{1}11)$ planes for all the HfO_2 films in order to obtain further information on the growth process, phase, and crystallite size at the nanoscale dimensions. It can be noted that the peak shifts to the higher diffraction angle for films grown from 200 °C to 400 °C. This trend continues for films grown at higher temperatures, however, at 500 °C the peak position retrogrades before continuing to increase. The shift in peak position is attributed to the lattice expansion and lattice mismatch between film and substrate. It is important to recognize the variation of d spacing for $(\bar{1}11)$ planes with T_s which aids in obtaining quantitative information on the lattice expansion. The d spacing versus T_s for HfO_2 films is shown in Figure 4.2. The trend in $d(\bar{1}11)$ is increasing for $T_s \leq 400$ °C, after which the trend begins to slightly decline for $T_s \geq 500$ °C. This leads to conclude that in this regime of T_s the lattice mismatch is at a maximum [3]. It is evident that at $T_s \geq 500$ °C,

the increase in grain size is affected more by the microstrain in the thin films, and slightly less by the effect of temperature. The average crystallite size increased from ~ 9 nm to ~ 18 nm with increasing T_s from 200 to 700 $^{\circ}\text{C}$. Furthermore, Figure 4.2 insinuates that the full width half maximum (FWHM) values decrease with T_s attributing to the increase in crystallite size, as per the Scherrer equation.

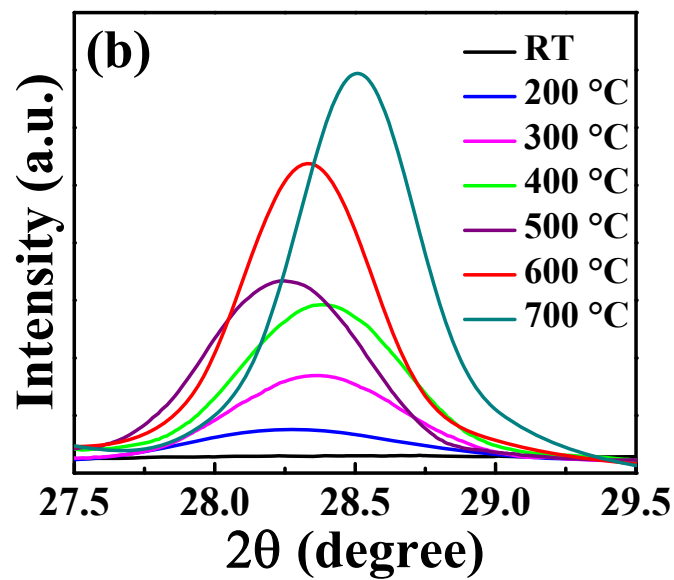
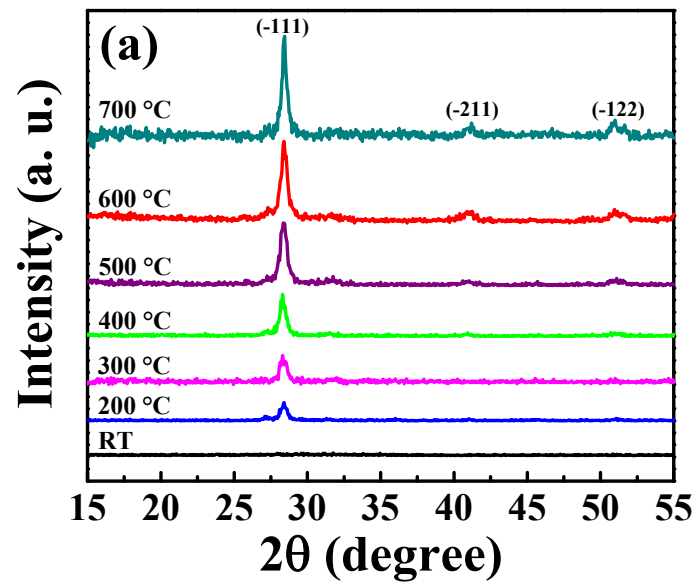


Figure 4.1 (a) GIXRD scans for HfO₂ films grown by variable temperature (b) High resolution scans of the ($\bar{1}11$) peaks obtained to assess further structural information.

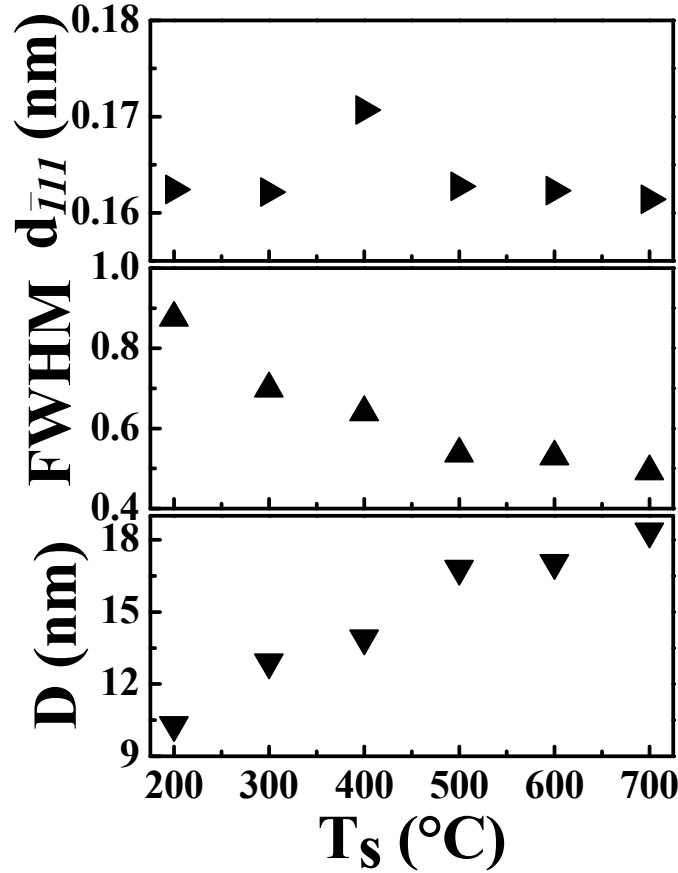


Figure 4.2 Crystallite size, FWHM, and d -spacing values obtained by fitting the high resolution ($\bar{1}11$) peaks with a Gaussian distribution.

4.2 Film Thickness and Density

To estimate thickness SEM cross-sectional analysis was performed on the HfO₂ films. Cross-sectional imaging provides information on the nucleation and growth of the HfO₂ thin films relative to the Si(100) substrate. The intrinsic growth behavior of HfO₂ will yield columnar grains perpendicular to the substrate [53]. The height of the columnar grains should be

representative of the thickness of the films [53]. Due to the strong insulating behavior of the films and very thin dimensions (< 50 nm), the columnar structure for the set of HfO_2 films employed in this investigation is not well resolved, although due to the contrast between film and substrate an adequate estimate of film thickness is achievable. Figure 4.3 demonstrates SEM cross-sectional images for $T_s = 500\text{-}600$ °C.

Simulation of the XRR experimental data using appropriate models can provide physiochemical information of HfO_2 films. Specifically, the surface roughness, thickness and density of the HfO_2 films can be obtained from XRR spectra. The density can be calculated from the total reflection or critical edge, while film thickness can be derived from the period of the oscillations in the XRR spectra. The stack model employed to simulate the XRR spectra contains, from top, HfO_2 film, SiO_2 interface and Si substrate (Fig. 4.4). The surface and interface roughness were also considered in order to accurately fit the experimental XRR spectra of HfO_2 films. The XRR data of HfO_2 films are shown in Figure 4.5. In the present case, it is evident that the experimental and simulation curves are in excellent agreement for the HfO_2 films. The fit parameters listed in Table 4.1 demonstrate the R-Factor and χ^2 values for the XRR experimental and simulated curves. The lesser values indicate a better agreement among simulated and experimental data. A positive shift of the critical edge noted from XRR spectra indicates that the film density increases with T_s ; further analysis was made with SE measurements as explained in the later portion of the discussion. The period of the oscillations present for the crystalline samples of the HfO_2 films does not significantly change with T_s , which conforms to the deposition rate to obtain ~ 40 nm thicknesses; thickness measurements will also be validated with SEM and SE measurements discussed below. Thickness measurements

observed were for the fully crystallized films ($T_s=300-700\text{ }^{\circ}\text{C}$). Structural information obtained for the HfO_2 films is demonstrated in Figure 4.6.

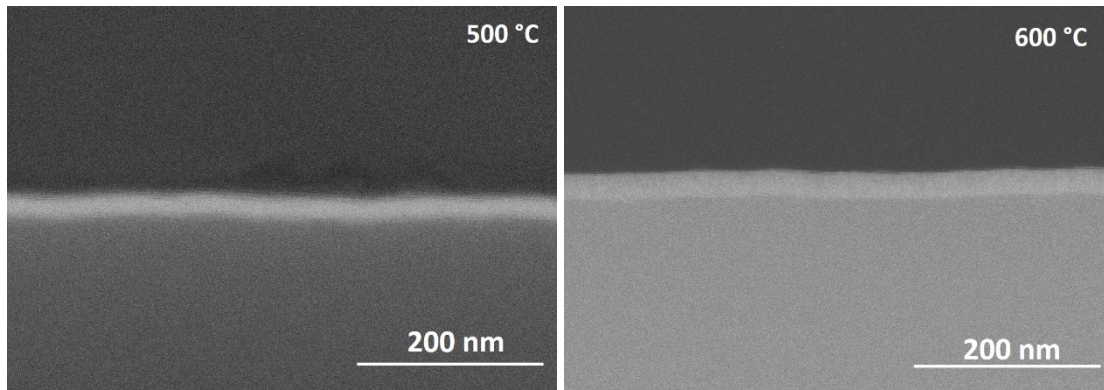


Figure 4.3 Cross-sectional imaging of the films obtained through electron microscopy to estimate direct film thickness.

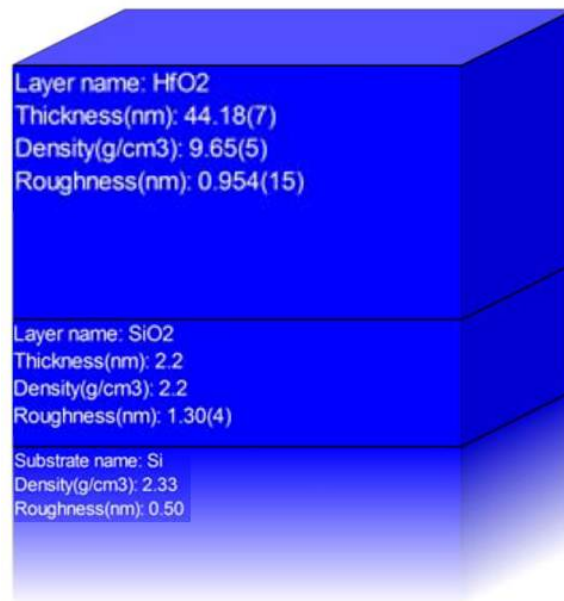


Figure 4.4 Layer model representative of the HfO_2 films; constructed for XRR data analysis.

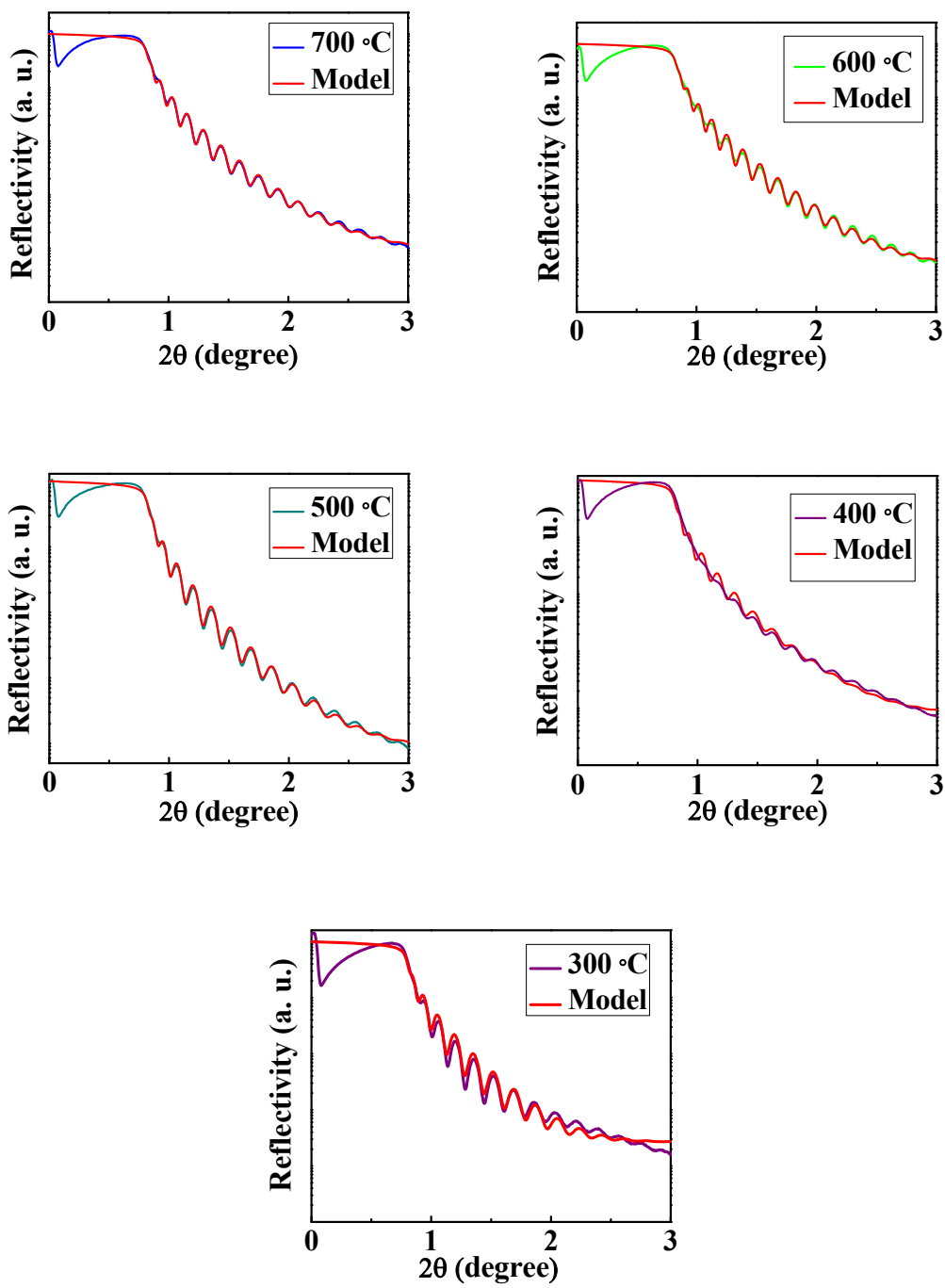


Figure 4.5 XRR spectra including experimental and model curves for the HfO_2 films grown at $T_s=300\text{-}700\text{ }^\circ\text{C}$.

T_s (°C)	300	400	500	600	700
R-Factor	0.048	0.03	0.02	0.027	0.019
χ^2	0.0153	0.00681	0.00283	0.00504	0.00244

Table 4.1 Fit parameters generated by using GlobalFit (Reflectivity Analysis).

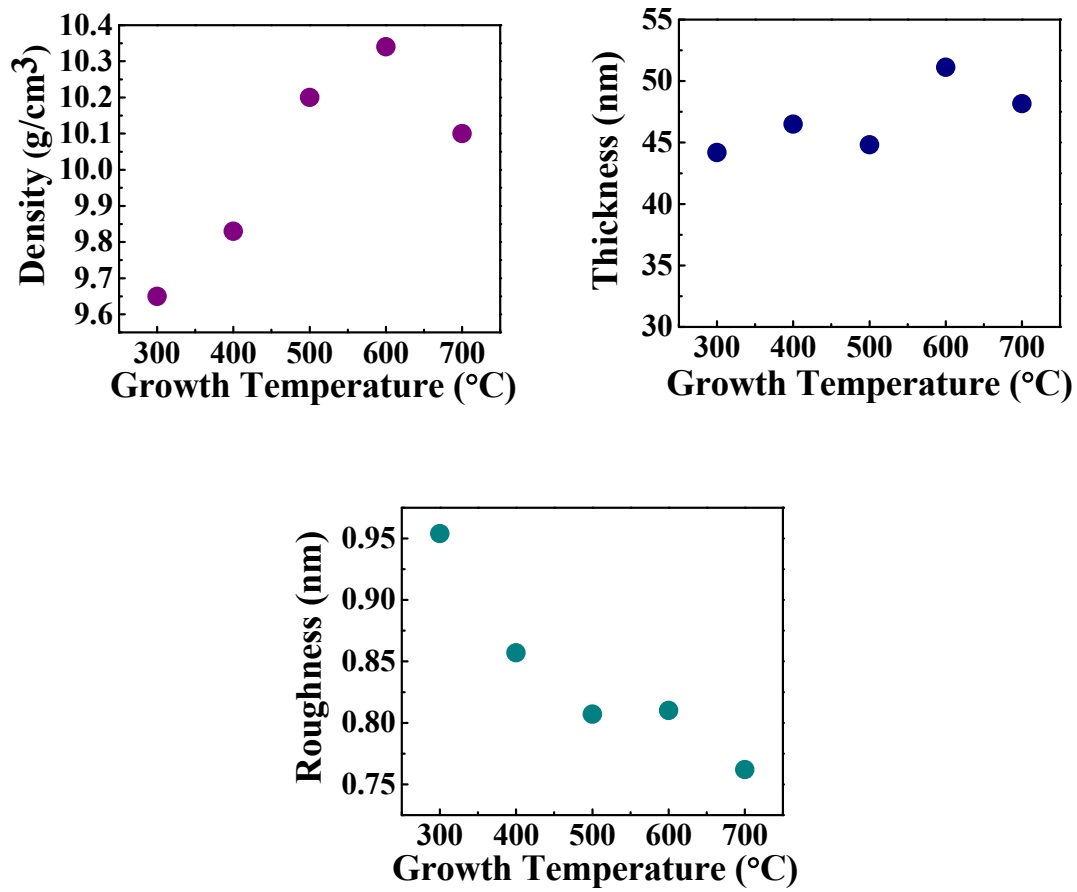
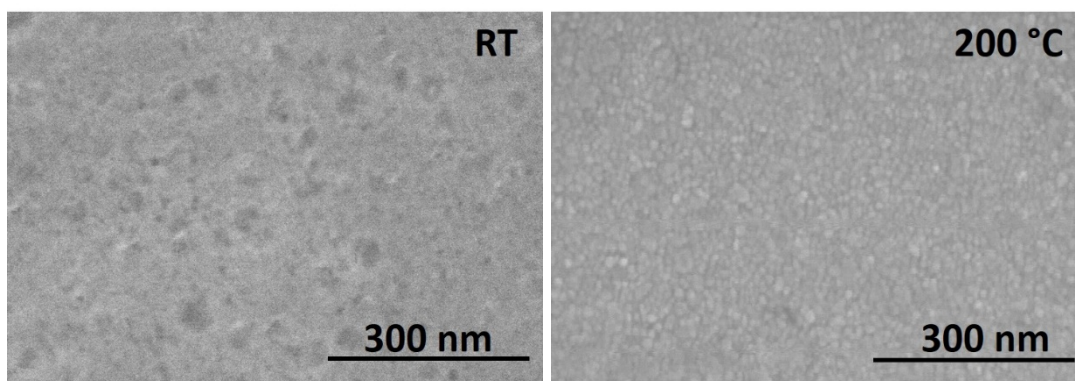


Figure 4.6 Density profile, thickness, and roughness values determined from XRR spectra for the crystalline HfO₂ films grown at T_s = 300 - 700 °C.

4.3 Surface Morphology

Scanning electron microscopy (SEM) images of the HfO_2 films are shown in Figure 4.7. The amorphous nature of the film is evident in the sample grown at RT. The crystalline samples ($T_s = 200\text{ }^\circ\text{C} - 700\text{ }^\circ\text{C}$) possess a uniform distribution of dense particles spherical in shape. Topographical features of the HfO_2 films are also correlated through AFM 2D imaging and shown in Figure 4.8. Most importantly, the 3D images (Fig. 4.9) provide an evident decrease in peak to valley or surface height with increase in growth temperature yielding a roughness profile as a function of temperature. The root-mean-square (rms) roughness of HfO_2 films decreases as T_s increases as seen in Figure 4.10. Roughness measurements are evidently related to the quality of the films. A smoother film will occupy fewer reaction sites and promote minimal interfacial reactions between the HfO_2 film and Si substrate. Figure 4.10 demonstrates a correlation between XRR roughness measurements and AFM roughness profiling which are well in agreement with one another.



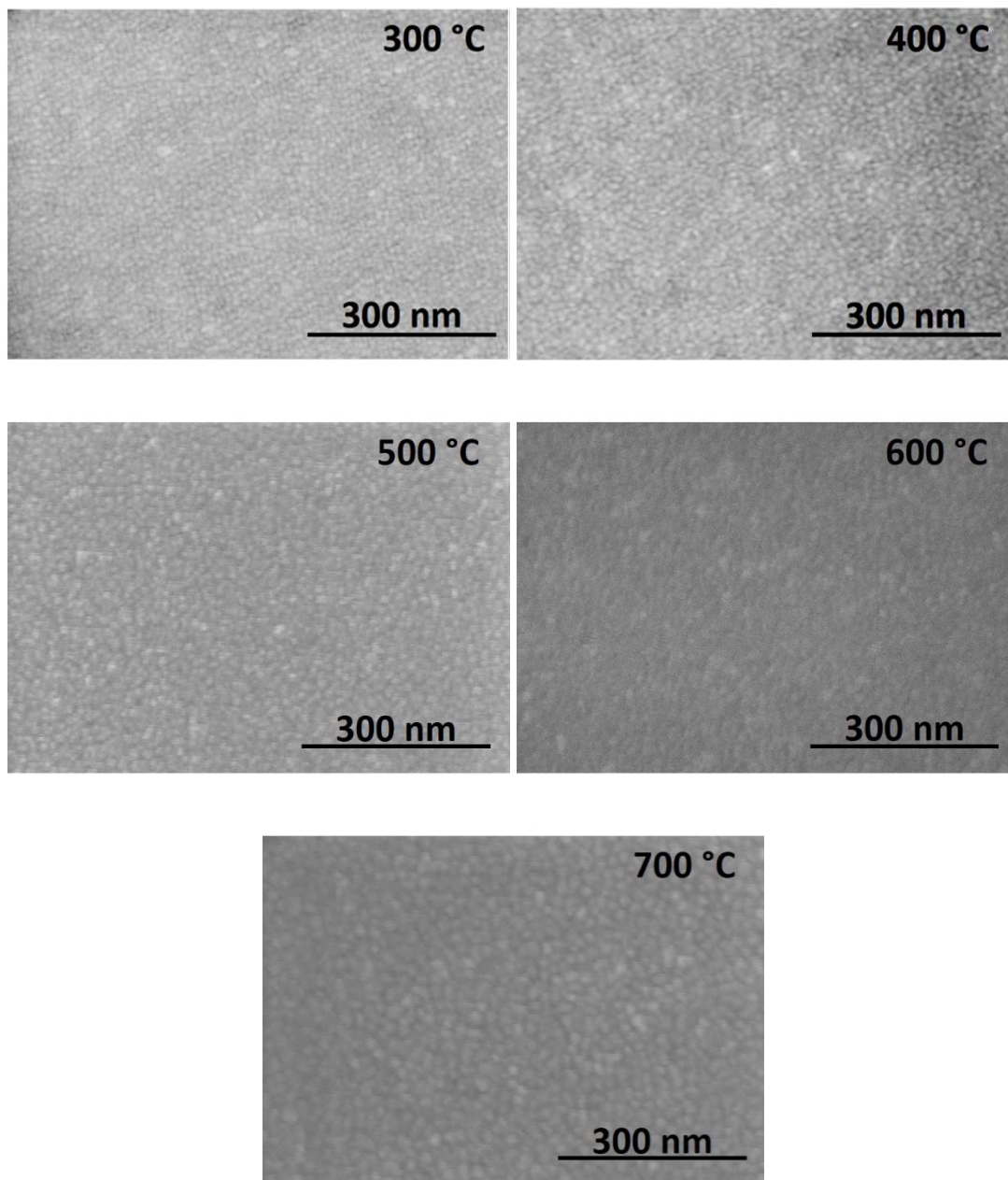


Figure 4.7 SEM surface images for the HfO_2 films grown as a function of T_s ; the polycrystalline films all entertain an equiaxed grain morphology at the nanoscale.

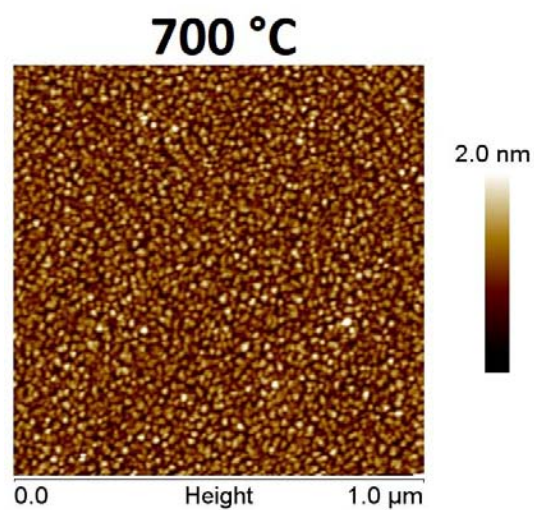
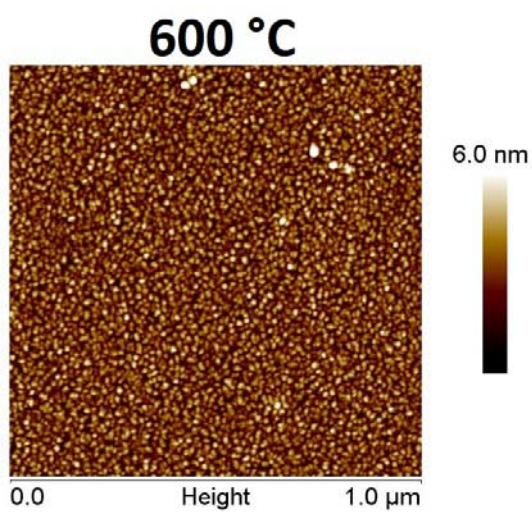
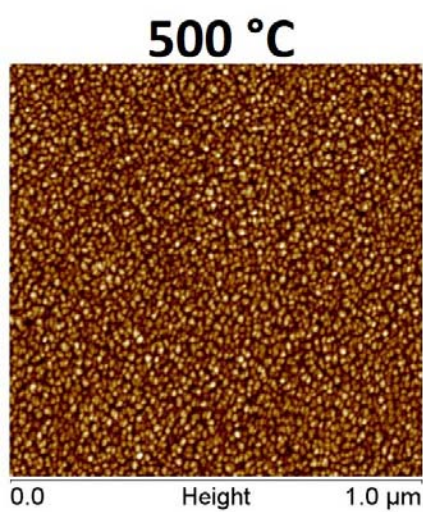
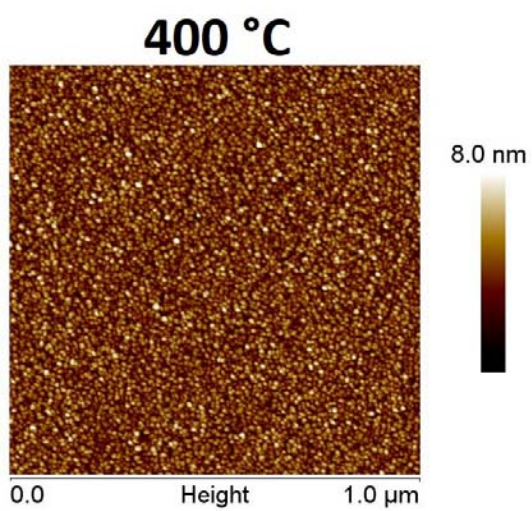
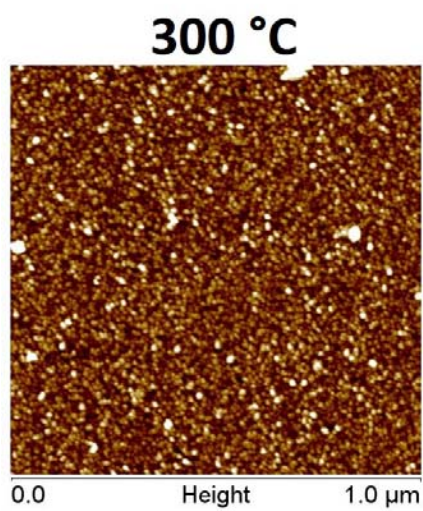
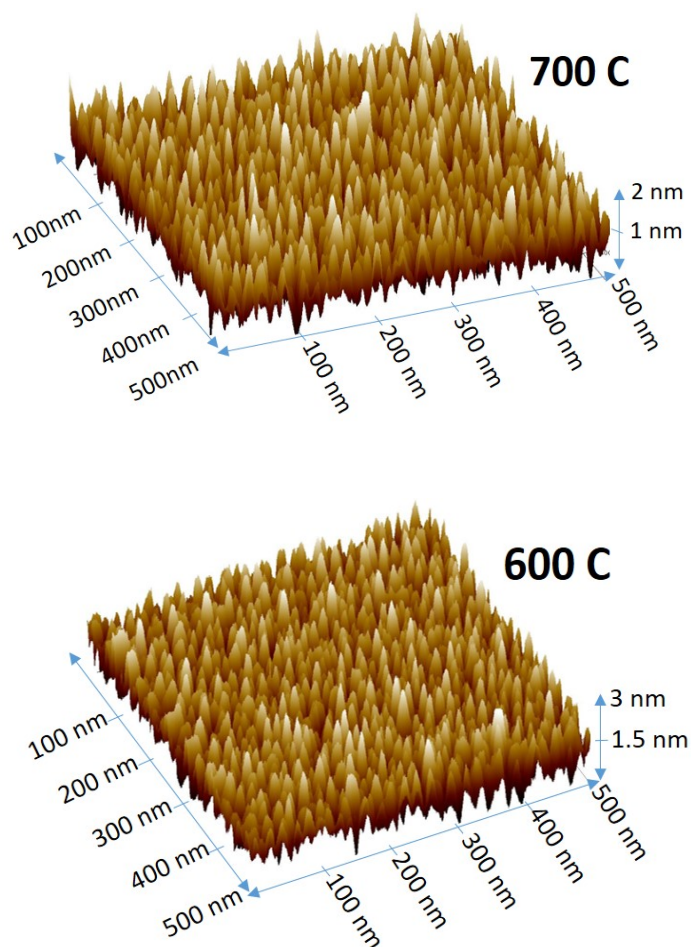


Figure 4.8 AFM surface images for the polycrystalline set of HfO_2 thin films; the crystallite morphology correlates with SEM.



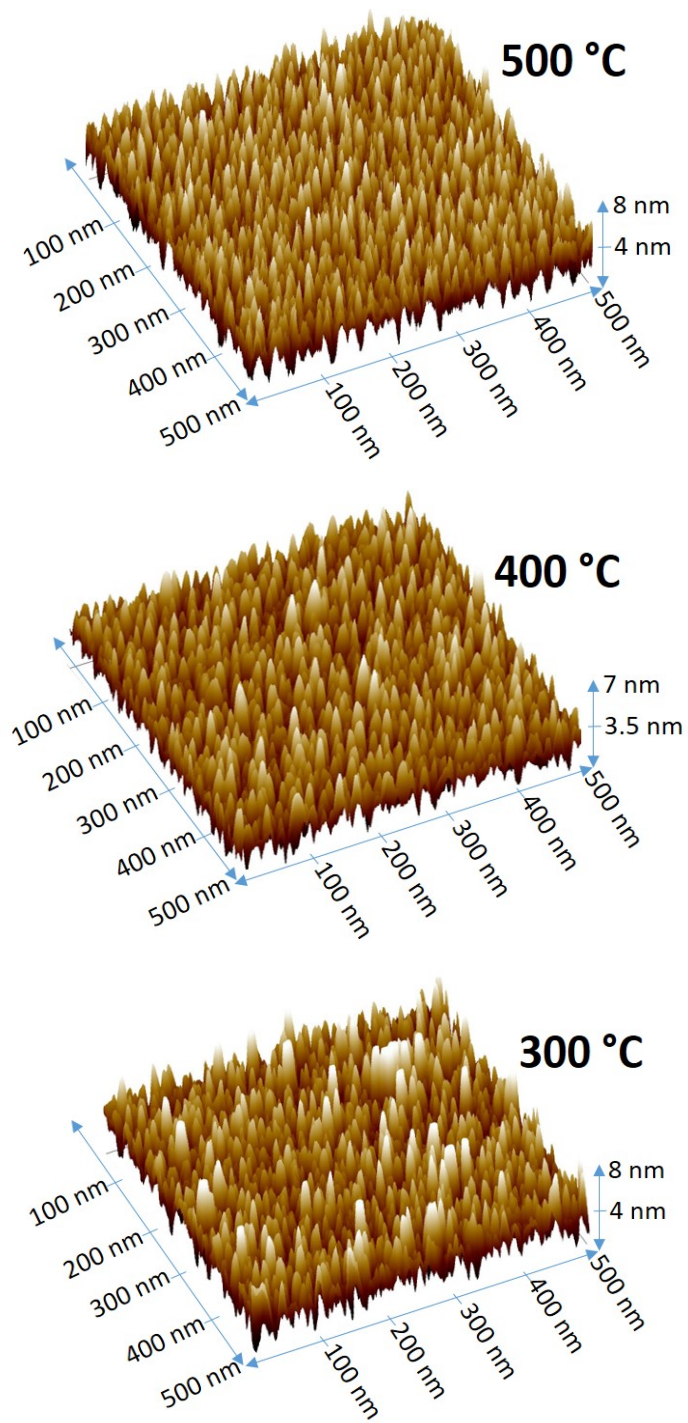


Figure 4.9 3D AFM images demonstrating an overall decrease in surface height with increasing

T_s .

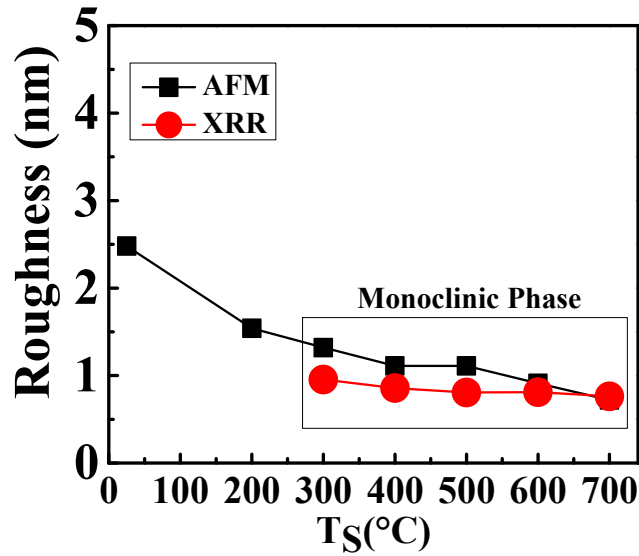


Figure 4.10 Roughness profile obtained by AFM imaging; superimposed are XRR roughness measurements for $T_s = 300 - 700$ °C.

4.4 Spectral Transmission Characteristics and Band Gap

Having established the microstructural and physical qualities of the HfO_2 films, the attention is now directed to the optical nature of the films. The spectral transmission spectra reveals that the HfO_2 films deposited on the quartz substrates were transparent and colorless down to the 200 nm wavelength range as seen in Figure 4.11. The highest transparency is provided by the amorphous film over a wide wavelength range (200 to 800 nm) ranging from 85% to 95% at lower wavelengths. The monoclinic polycrystalline films still employ transparencies of near 70% at lower wavelengths but significantly less than the amorphous film. Evidently, the contribution of amorphous to monoclinic phase transition and structural ordering has a vast impact on the optical nature of the films. A further analysis of the optical spectra is performed to better understand the effect of microstructure on the optical properties and to derive

a quantitative structure-property relationship [54]. The optical absorption coefficient, α , of the films is evaluated using the relation:

$$\alpha = -[1/t] \ln[T / (1 - R)^2] \quad (10)$$

where T is the transmittance, R is the reflectance, and t is the film thickness [54-58]. Absorption data for the films grown at $T_s = RT - 700$ °C can be seen in Figure 4.12. An interesting observation to be made from the absorption data is the shoulder-like feature provided by the crystalline films. The visible shoulder becomes prominent after the phase transition from amorphous to monoclinic, similar observations have been reported by Park *et al.* and Cisneros-Morales and Aita [30,56]. Cisneros-Morales and Aita justified the phenomena as a band that initiates and saturates below E_g of the films but develops definition with increase in temperature [30]. The existence of the additional absorption band is arguable among other reports that encounter the same features in HfO_2 . The additional band feature is said to be attributed to defects such as oxygen vacancies in the lattice of HfO_2 or other structure related defects, which will undoubtedly alter the optical behavior [30,56-57].

The absorption data is studied to analyze the nature and value of the band gap (E_g) [54-59]. A direct band gap follows the power law of the form:

$$\alpha h\nu = A(h\nu - E_g)^n \quad (11)$$

where $h\nu$ is the incident photon, α is the absorption coefficient, A is the absorption edge width parameter, and n is the exponent [54-59]. When there is a direct band gap a plot of $(\alpha h\nu)^2$ versus $h\nu$ would have a linear region with slope A, whose extrapolation to $\alpha(h\nu) = 0$ would give the value of E_g [59]. An indirect transition for E_g follows the power law or Tauc law of the form:

$$\sqrt{(\alpha h\nu)} = B_{Tauc}(h\nu - E_g) \quad (12)$$

where B_{Tauc} is the Tauc parameter or the slope of the linear region when $h\nu$ is plotted as a function of $(\alpha h\nu)^{1/2}$ [59]. The indirect band gap value for HfO_2 is related to the electronic transition from the O 2p valence band to the Hf 5d conduction band between Γ and B points on the reciprocal lattice of monoclinic HfO_2 [5,30,56,61]. However, looking at the absorption coefficient for the films exhibiting monoclinic orientations ($T_s = 200 - 600^\circ\text{C}$) at values higher than 6.00 eV (Fig. 4.12) the steepest increase in absorption is observed. The high energies coupled with high absorption behavior tailor to band-band transitions, and therefore E_g has been measured by following the direct band gap power law [57-60]. Extrapolating the linear region of the plot to zero and regression analysis for R^2 values greater than 0.9 provide accurate E_g values as seen in Figure 4.13. The band gap values are increasing with increasing T_s as observed in Figure 4.14 in the range of 5.75 to 6.19 eV.

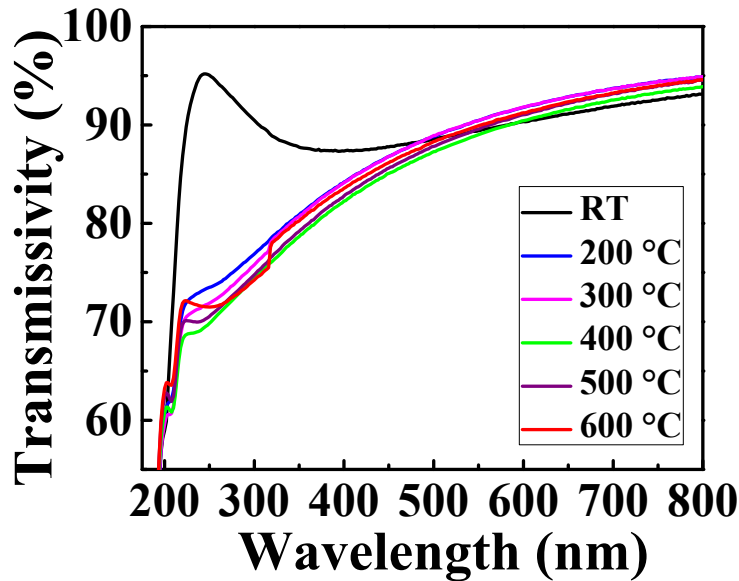


Figure 4.11 Transmission spectra for the HfO_2 films.

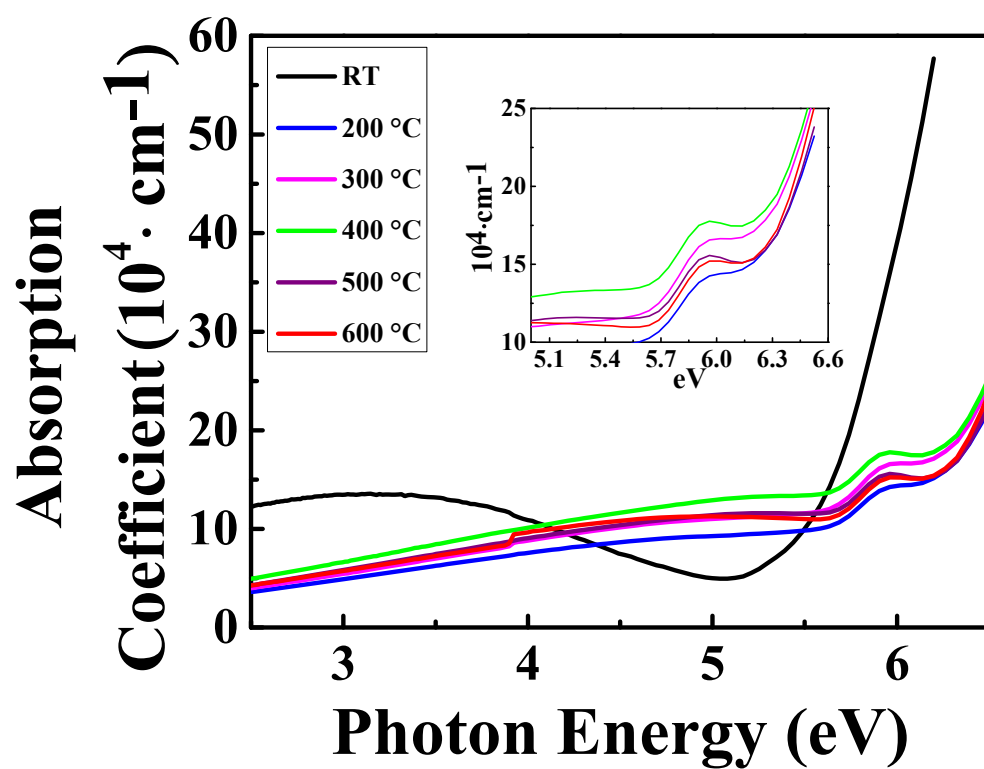
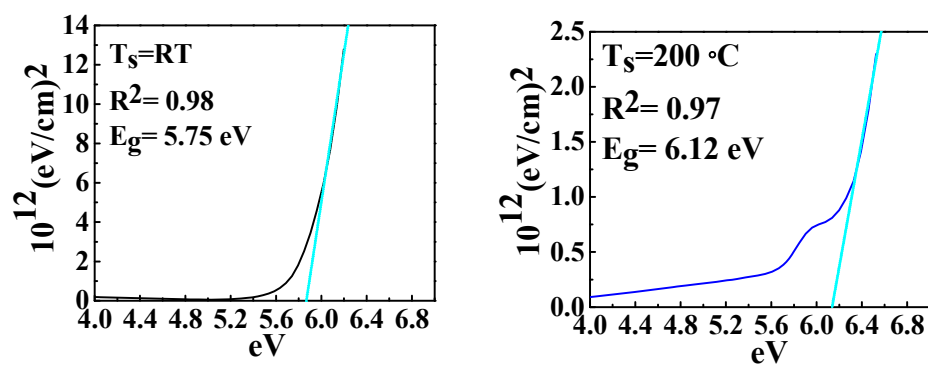


Figure 4.12 Absorption coefficient, α , as a function of photon energy for HfO₂ films.



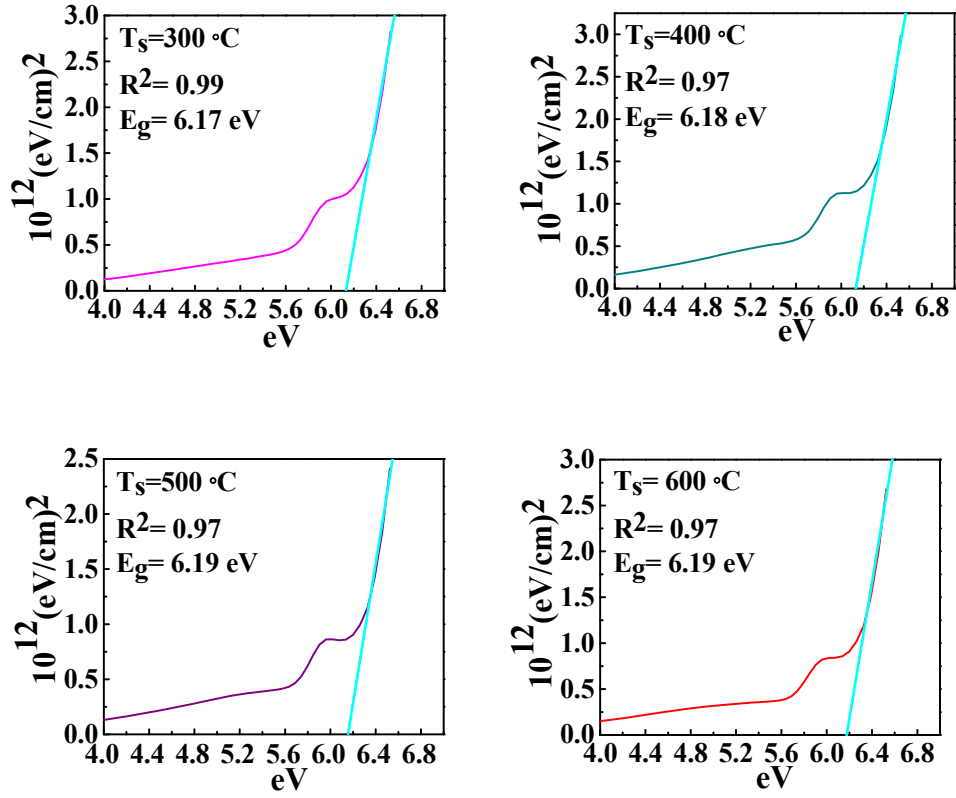


Figure 4.13 $(\alpha h\nu)^2$ as a function of photon energy for the HfO_2 films grown at $T_s = \text{RT} - 600^\circ\text{C}$.

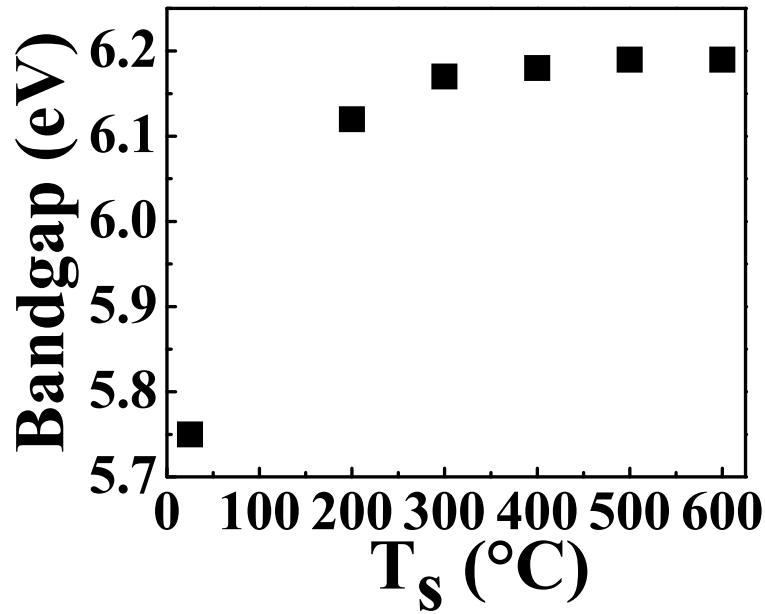


Figure 4.14 Summarized band gap values as a function of T_s .

4.5 Optical Constants

Ultimately, the optical constants of the nanocrystalline, monoclinic HfO_2 films are considered and discussed. The stack model constructed for SE data fitting was composed of the Si substrate, an interfacial SiO_2 layer, and the HfO_2 films; the surface roughness was also considered to obtain precision during experimental fitting. Figure 4.15 represents the optical model used for the HfO_2 films. The spectral dependencies of the experimental parameters obtained from SE measurements, Ψ and Δ are plotted in Figure 4.16 for the HfO_2 films on Si(100) substrates. The curves obtained for HfO_2 films indicate a reasonable agreement between experimental and simulated data; the MSE values are listed in Table 4.2. The behavior of the curves is highly influenced by the variable growth temperature, and further characterized through the optical constants.

Microstructural information obtained from SE data for the HfO_2 films is film thickness, which is relative to the stack optical model. The variation of film thickness as a function of growth temperature for various crystalline HfO_2 films is shown in Figure 4.17. It is evident that the film thickness is more or less constant with increasing growth temperature; this observation is consistent with XRR for the crystalline samples. To validate the SE analysis and microstructure, the film thickness values obtained from SEM measurements are also plotted in Figure 4.17. Distinct film properties are responsible for film thickness characterization, and ultimately it can be seen that the film thickness obtained from SE, XRR, and SEM are in reasonable agreement with respect to one another for the monoclinic HfO_2 films. This observation indicates that the model(s) and SE analysis adopted can reasonably simulate the microstructure and, hence, optical properties of the sputter-deposited HfO_2 films.

The dispersion profiles of $n(\lambda)$ determined from SE data for the HfO_2 films are shown in Figure 4.18. The $n(\lambda)$ dispersion curves indicate a sharp increase at shorter wavelengths corresponding to fundamental absorption of energy across the band gap. However, the effect of growth temperature is evident in the dispersion curves (Fig. 4.18), where there is an increase in ' n ' with T_s . In order to further study the effect of growth temperature on the optical constants, the refractive index variation of the films at $\lambda = 550$ nm with growth temperature is extracted and demonstrated as function of T_s in Figure 4.19. At a $\lambda=550$ nm, the ' n ' values increase from 1.79 to 2.09 with increasing growth temperature from 25 to 700 °C. The temperature dependence on structure is evident in the measurements where ' n ' values increase drastically between the amorphous and monoclinic transformation of HfO_2 . Note that the ' n ' values increase sharply with T_s initially and begin to depend less at higher T_s , a characteristic that correlates with structural GIXRD data analysis. However, the values obtained for the films are slightly less than the reported bulk value for HfO_2 which can be attributed to the method of growth; the sputtered films are well known to have a higher defect density than bulk HfO_2 .

Evident from the results and analysis, the optical quality of the HfO_2 films depends on the growth temperature and, hence, the film-microstructure. A simple model can be formulated to explain the effect of microstructure on the optical properties in HfO_2 films. XRD measurements demonstrated that the HfO_2 films grown at $T_s=RT-700$ °C exhibit two sets of broad features from a structure point of view: amorphous and nanocrystalline. The nanocrystalline HfO_2 films crystallize in monoclinic structure. Furthermore, increasing T_s results in improved structural order and texturing of HfO_2 films along with an increase in the average crystallite size. The density of the film also increases, as evidenced by XRR analyses. It is well known that the refractive index is closely related to the physical properties and density of the films. Thus, the

observed increase in ‘ n ’ values when HfO₂ films grown at higher T_s can be attributed to the improved packing density of the films coupled with improved structural ordering. Improved structural ordering results in the formation of a dense network of nanocrystals leading to an enhancement in the packing density. This characteristic change in structure results in the observed improvement in ‘ n ’. In order to further confirm the proposed physics and mechanism, the relative density of the film is also approximated using the Lorentz-Lorenz relation employing the measured ‘ n ’ values at 550 nm [67-68]. The Lorentz-Lorenz relation states the following:

$$\frac{\rho_f}{\rho_b} = \frac{(n_f^2 - 1)(n_b^2 + 2)}{(n_f^2 + 2)(n_b^2 - 1)} \quad (13)$$

where ρ_f / ρ_b is the relative density, f and b differ between film and bulk material, respectively [68]. The functional dependence of the relative density of HfO₂ films on T_s is shown in Figure 4.20. The density measured for amorphous HfO₂ films at T_s =RT is only 7.4 g/cm³. However, the density increases to 9.1 g/cm³ for nanocrystalline HfO₂ films deposited at T_s =300-700 °C. XRR density measurements commensurate with the values derived from Lorentz-Lorenz relation as seen for the crystalline samples in the inset within Figure 4.20.

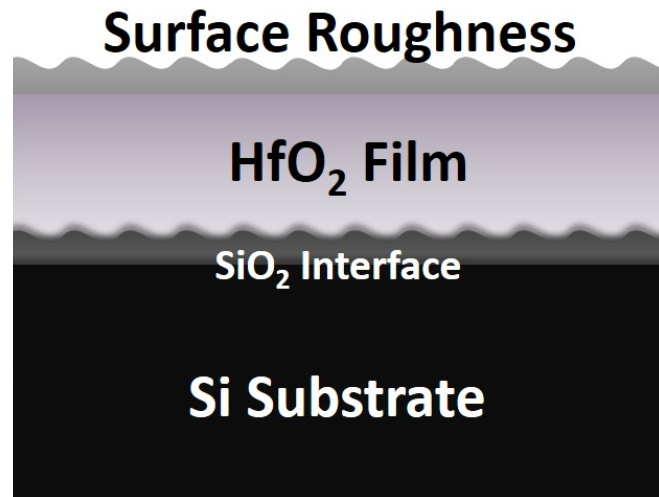
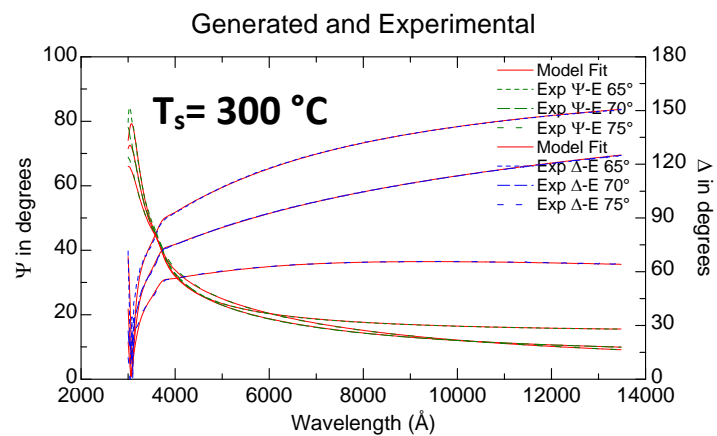
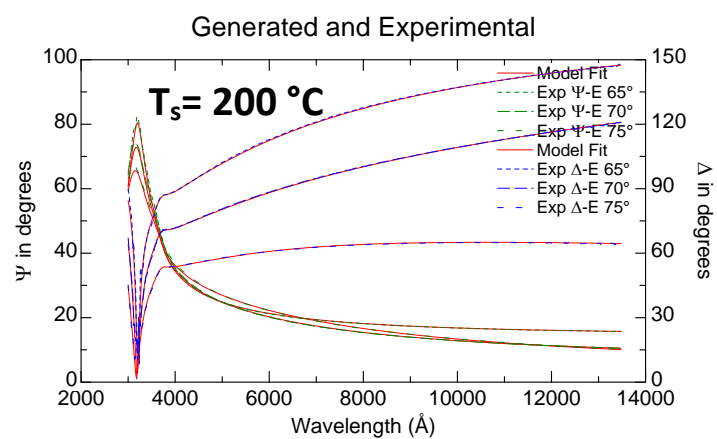
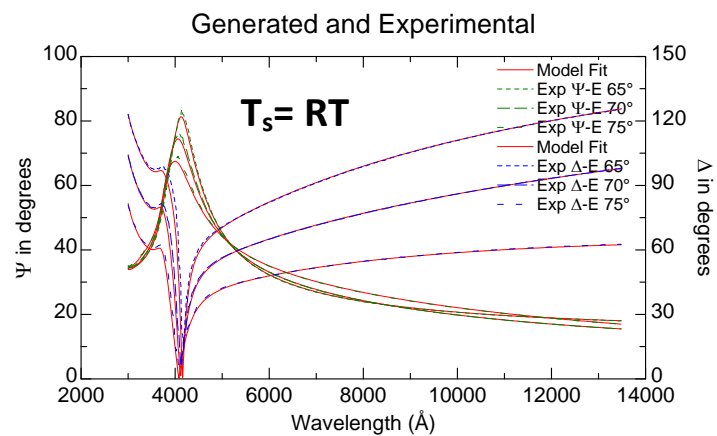
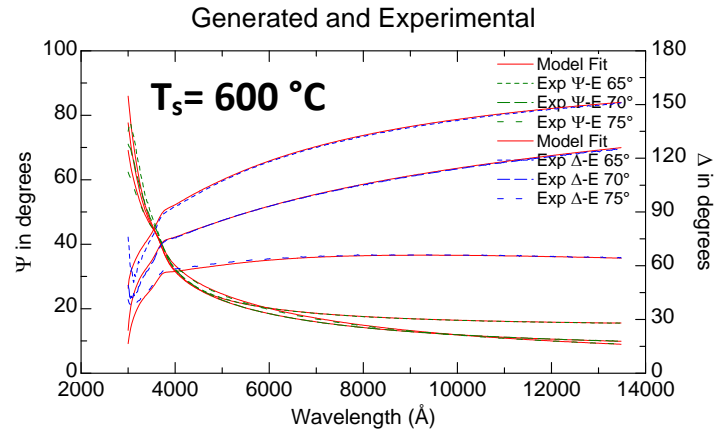
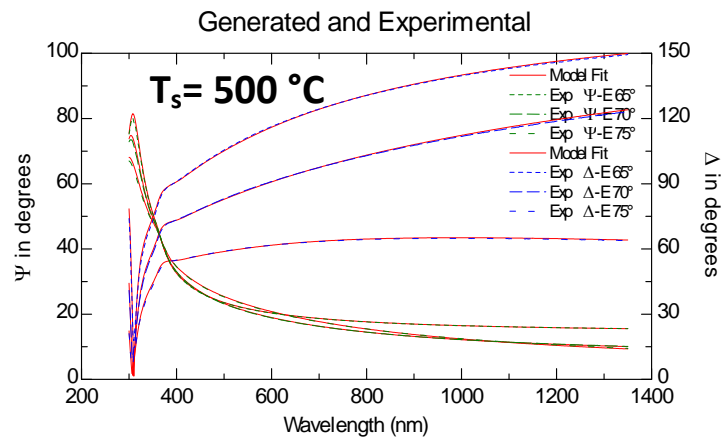
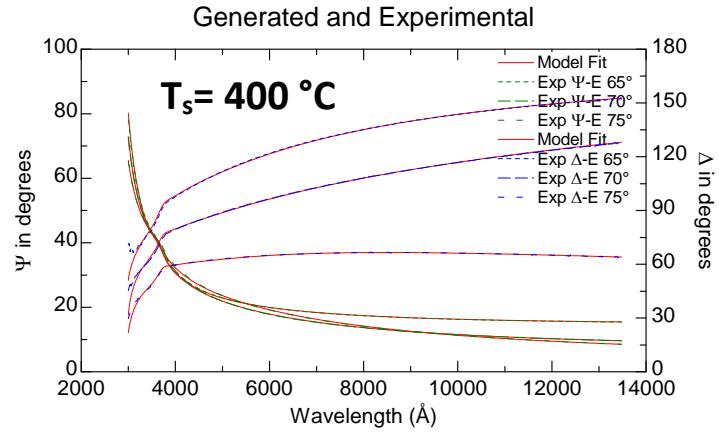


Figure 4.15 Optical stack model employed for SE data analysis.





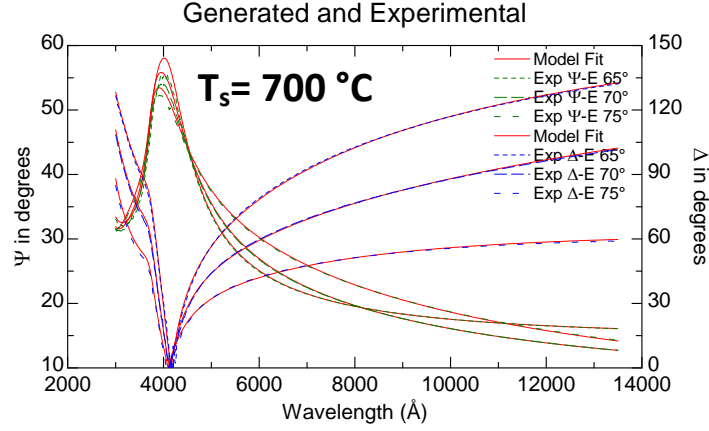


Figure 4.16 The spectral dependencies of Ψ and Δ along with the simulated data constructed from the optical model for HfO_2 films.

T_s (°C)	<i>RT</i>	<i>200</i>	<i>300</i>	<i>400</i>	<i>500</i>	<i>600</i>	<i>700</i>
<i>MSE</i>	3.379	4.059	2.98	2.999	5.603	6.255	3.194

Table 4.2 Mean-squared error values from the quality of the match between the data calculated from the model and the experimental data.

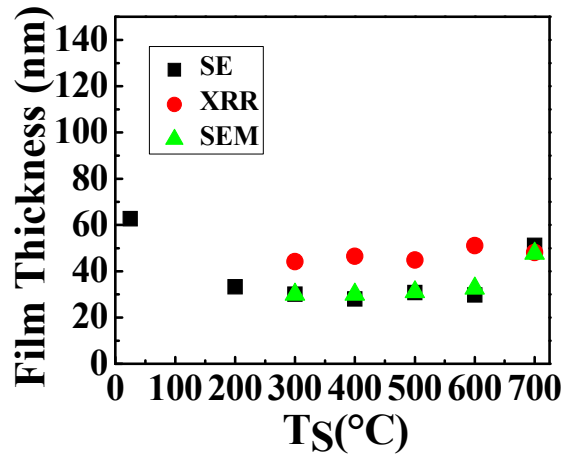


Figure 4.17 Film thickness measurements, measured directly through SEM, and by data fitting for XRR and SE analysis.

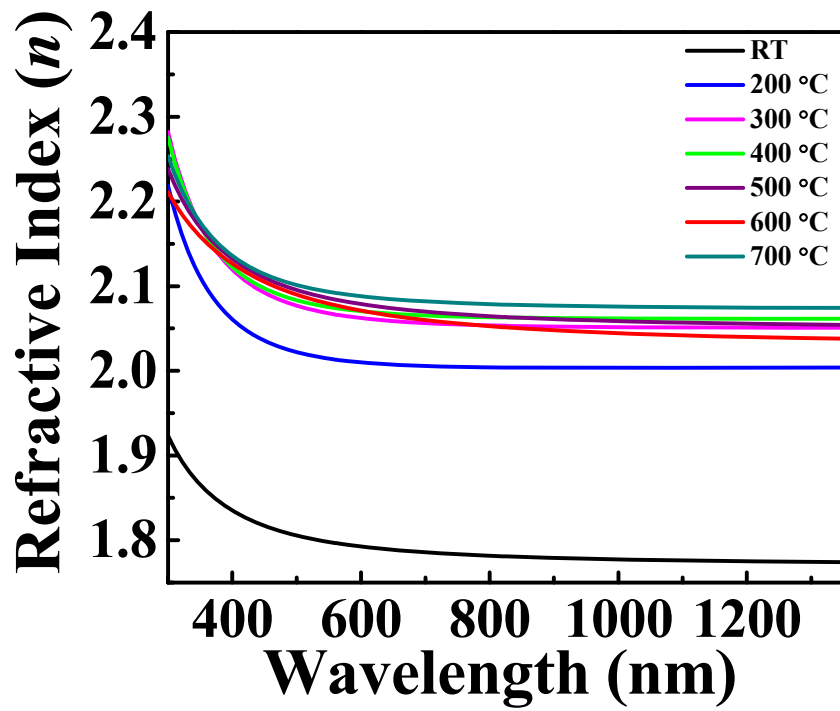


Figure 4.18 Index of refraction as a function of wavelength (300 – 1350 nm).

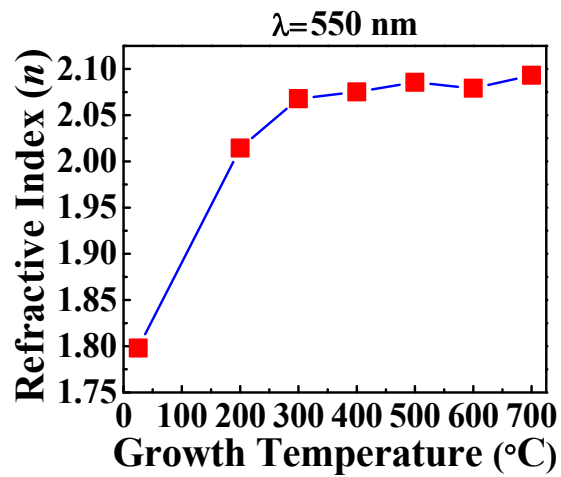


Figure 4.19 ‘ n ’ values extracted at $n(550)$ to understand as a function of T_s .

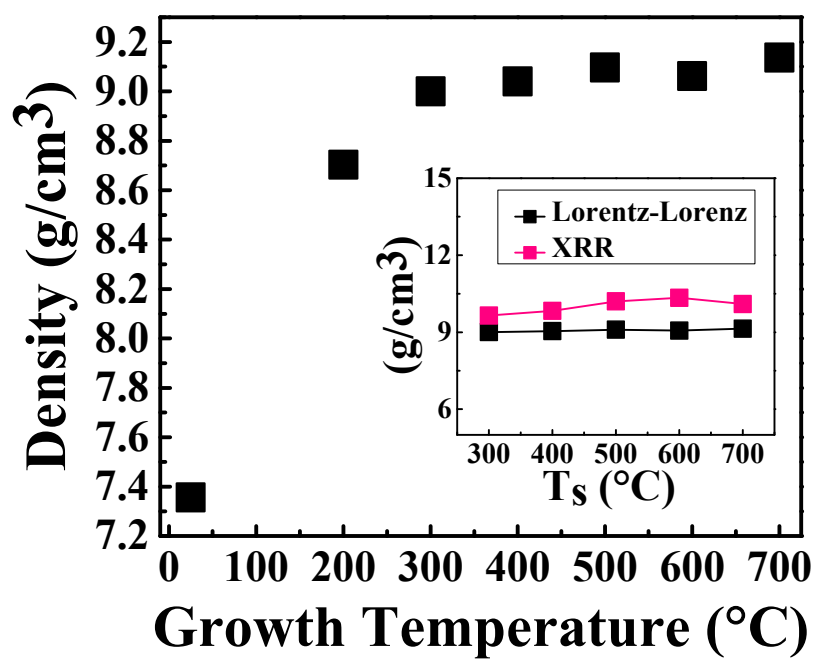


Figure 4.20 Density measurements approximated through the Lorentz-Lorenz relation and compared to XRR derived measurements.

Chapter 5: Conclusions

Nanocrystalline HfO_2 films were fabricated using sputter-deposition by varying deposition temperature. Structural and optical properties were investigated in order to derive a nanometric structure-property relationship. Microstructural details obtained from GIXRD indicate a crystallization temperature for monoclinic HfO_2 at 200 °C. Further increase in T_s results in increased diffraction intensity implying a growth in crystallite size, and is confirmed by SEM and AFM analyses. Microstructural information such as film thickness was successfully derived through XRR, SEM and SE data, and ultimately indicate that these are highly qualified characterization methods for structural film information. The optical behavior of the films was probed through spectrophotometry and spectroscopic ellipsometry measurements. The results indicate that the HfO_2 films grown at $T_s = \text{RT} - 700$ °C are highly transparent and exhibit low optical losses in the visible and near infrared regions. The quality of the film was also studied through SE measurements, specifically using the $n(\lambda)$ dispersion profile along with the well-known Lorentz-Lorenz relation to obtain film density and relative density. The films were highly dense possessing high index of refraction values. The increase in density correlates to the increase in index of refraction for the films, a consequence of growth temperature dependence on film formation. Furthermore, it was achievable to manipulate the resulting film properties based on the fabrication conditions by variable growth temperature.

Chapter 6: Future Work

- Further explore HfO_2 films for construction and design of an optical device.
- Build a multilayer optical mirror consisting of dielectric/metal/dielectric for antireflective applications.
- Tailor the index of refraction for HfO_2 films to be used in the multilayer optical mirror, in order to cover a wide spectral region.
- Explore the hafnium-oxy-nitride behavior in comparison to HfO_2 films.
- Develop a post-deposition anneal to incorporate nitrogen into HfO_2 by utilizing ammonia gas.

References

- [1] Jaffe, J.E.; Bachorz, R.A.; Gutowski, M. Low-temperature polymorphs of ZrO_2 and HfO_2 : A density-functional theory study, *Physical Review B*, **2005**, 72, 114107-1-9.
- [2] Hann, R.E.; Suitch, P.R.; Pentecost, J.L. Monoclinic Crystal Structures of ZrO_2 and HfO_2 refined from x-ray powder diffraction data, *Journal of the American Ceramic Society*, **1985**, 68, C-285-C-286.
- [3] Ramana, C.V.; Kamala Bharathi, K.; Garcia, A.; Campbell, A.L. Growth behavior, lattice expansion, strain, and surface morphology of nanocrystalline monoclinic HfO_2 thin films, *The Journal of Physical Chemistry C*, **2012**, 116 (18), 9955-9960.
- [4] K. Momma and F. Izumi, "VESTA 3 for three-dimensional visualization of crystal, volumetric and morphology data," *Journal of Applied Crystallography*, **2011**, 44, 1272-1276.
- [5] Demkov, A.A.; Navrotsky, A. *Materials Fundamentals of Gate Dielectrics*, Springer, **2005**, 256.
- [6] Greer, J.; Korkin A.; Labanowski, J. *Nano and Giga Challenges in Microelectronics*, Elsevier B. V., **2003**, 164-167.
- [7] Ruh, R.; Corfield, P.W.R. Crystal structure of monoclinic hafnia and comparison with monoclinic zirconia, *Journal of the American Ceramic Society*, **1970**, 53, 126-129.
- [8] Okamoto, H. Hf-O (Hafnium-Oxygen), *Journal of Phase Equilibria and Diffusion*, **2008**, 29, 124.
- [9] Kang, J.; Lee, E.-C.; Chang, K.J. First-principles study of the structural phase transformation of hafnia under pressure, *Physical Review B*, **2003**, 68, 054106-1.

- [10] Desgreniers, S.; Lagarec, K. High-density ZrO_2 and HfO_2 : Crystalline structures and equations of state, *Physical Review B*, **1999**, 59, 8467-8472.
- [11] Ortega, A.; Rubio, E.J.; Abhilash, K.; Ramana, C.V. Correlation between phase and optical properties of yttrium-doped hafnium oxide nanocrystalline thin films, *Optical Materials*, **2013**, 35, 1728-1734.
- [12] Bright, T.J.; Watjen, J.I.; Zhang, Z.M.; Muratore, C.; Voevodin, A.A. Optical properties of HfO_2 thin films deposited by magnetron sputtering: From the visible to the far-infrared, *Thin Solid Films*, **2012**, 520, 6793-6802.
- [13] Willey, R.R. *Practical Design and Production of Optical Thin Films*, Marcel-Dekker, **2002**, 280-281.
- [14] Al-Kuhaili, M.F. Optical properties of hafnium oxide thin films and their application in energy-efficient windows, *Optical Materials*, **2004**, 27, 383-387.
- [15] Torchio, P.; Gatto, A.; Alvisi, M.; Albrand, G.; Kaiser, N.; Amra, C. High-reflectivity $\text{HfO}_2/\text{SiO}_2$ ultraviolet mirrors, *Applied Optics*, **2002**, 41, 3256-3261.
- [16] Zukic, M.; Torr, D.G.; Spann, J.F.; Torr, M.R. Vacuum ultraviolet thin films. 1: Optical constants of BaF_2 , CaF_2 , LaF_3 , MgF_2 , Al_2O_3 , HfO_2 , and SiO_2 thin films, *Applied Optics*, **1990**, 29, 4284-4292.
- [17] Hildebrandt, E.; Kurian, J.; Zimmerman, J.; Fleissner, A.; von Seggem, H.; Alff, L. Hafnium oxide thin films: Effect of growth parameters on oxygen and hafnium vacancies, *Journal of Vacuum Science and Technology B*, **2009**, 27, 325-328.
- [18] Choi, J.H.; Mao, Y.; Chang, J.P. Development of hafnium based high-k materials-A review, *Materials Science & Engineering R*, **2011**, 72, 97-136.

- [19] Wilk, G.D.; Wallace, R.M.; Anthony, J.M. High-k gate dielectrics: Current status and materials properties considerations, *Journal of Applied Physics*, **2001**, 89, 5243-5275.
- [20] Robertson, J. Interfaces and defects of high-*K* oxides on silicon, *Solid-State Electronics*, **2005**, 49, 283-293.
- [21] Ran, J.; Yan Z. Observation of ferromagnetism in highly oxygen-deficient HfO₂ films, *Journal of Semiconductors*, **2009**, 30, 102002-1-5.
- [22] Coey, J.M.D.; Venkatesan, P.; Stamenov, C.; Fitzgerald, C.B.; Dorneles, L.S. Magnetism in hafnium dioxide, *Physical Review B*, **2005**, 72, 024450-1-6.
- [23] Opeka, M.M.; Talmy, I.G.; Wuchina, E.J.; Zaykoski, J.A.; Causey, S.J. Mechanical, thermal, and oxidation properties of refractory hafnium and zirconium compounds, *Journal of the European Ceramic Society*, **1999**, 19, 2405-2414.
- [24] Pearson, H.O. *Handbook of Chemical Vapor Deposition, 2nd Edition: Principles, Technology, and Application*, Noyes Publication, NY, **1999**, 240.
- [25] Dave, V.; Dubey, P.; Gupta, H.O.; Chandra, R. Effect of sputtering gas on structural, optical, and hydrophobic properties of DC-sputtered hafnium oxide thin films, *Surface Coatings & Technology*, **2013**, 232, 425-431.
- [26] Ma, C.Y.; Wang, W.J.; Wang, J.; Miao, C.Y.; Li, S.L.; Zhang, Q.Y. Structural, morphological, optical, and photoluminescence properties of HfO₂ thin films, *Thin Solid Films*, **2013**, 545, 279-284.
- [27] Szymanska, M.; Gieraltowska, S.; Wachnicki, L.; Grobelny, M.; Makowska, K.; Mroczynski, R. Effect of reactive magnetron sputtering parameters on structural and electrical properties of hafnium oxide thin films, *Applied Surface Science*, **2014**, xx, xxx-xxx.

- [28] Maidul Haque, Sk.; Sagdeo, P.R.; Balaji, S.; Sridhar, K.; Kumar, S.; Bhattacharyya, D.; Bhattacharyya, D.; Sahoo, N.K. Effect of substrate bias and oxygen partial pressure on properties of RF magnetron sputtered HfO₂ thin films, *Journal of Vacuum Science and Techonology*, **2014**, 32, 03D104-1-9.
- [29] Khoshman, J.M.; Khan, A.; Kordesch, M.E. Amorphous hafnium oxide thin films for antireflection optical coatings, *Surface Coatings & Technology*, **2008**, 202, 2500-2502.
- [30] Cisneros-Morales, M.C.; Aita C.R. The effect of nanocrystalline size in monoclinic HfO₂ films on lattice expansion and near-edge optical absorption, *Applied Physics Letters*, **2010**, 96, 191904-1-3.
- [31] Liu, M.; Fang, Q.; He, G.; Zhu, L.Q.; Zhang, L.D. Characterization of HfO_xN_y dielectrics using hafnium oxide as a target, *Applied Surface Science*, **2006**, 252, 8673-8676.
- [32] Aguirre, B.; Vemuri, R.S.; Zubia, D.; Engelhard, M.H.; Shutthanadan, V.; Kamala Bharathi, K.; Ramana, C.V. Growth, microstructure and electrical properties of sputter-deposited hafnium oxide (HfO₂) thin films grown using a HfO₂ ceramic target, *Applied Surface Science*, **2011**, 257, 2197-2202.
- [33] Durrani, S.M.A.; CO-sensing properties of hafnium oxide thin films prepared by electron beam evaporation, *Sensors & Actuators B: Chemical*, **2007**, 120, 700-705.
- [34] Callegari, A.; Cartier, E.; Gribelyuk, M.; Okorn-Schmidth, H.F.; Zabel, T. Physical and electrical characterization of Hafnium oxide and Hafnium silicate sputtered films, *Journal of Applied Physics*, **2001**, 90, 6466-6475.
- [35] Pereira, L.; Barquinha, P.; Fortunato, E.; Martins, R. Influence of the oxygen/argon ratio on the properties of sputtered hafnium oxide, *Materials Science & Engineering B*, **2005**, 118, 210-213.

- [36] Tan, T.; Liu, Z.; Lu, H.; Liu, W.; Tian H. Structure and optical properties of HfO₂ thin films on silicon after rapid thermal annealing, *Optical Materials*, **2010**, 32, 432-435.
- [37] Hu, H.; Zhu, C.; Lu, Y.F.; Wu, Y.H.; Liew, T.; Li, M.F.; Cho, B.J.; Choi, W.K.; Yakovlev, N. Physical and electrical characterization of HfO₂ metal-insulator-metal capacitors for Si analog circuit applications, *Journal of Applied Physics*, **2003**, 94, 551-557.
- [38] Jones, J.R.; Clare, A.G. *Bio-Glasses: An Introduction*, John Wiley & Sons Ltd., United Kingdom, **2012**.
- [39] Nalwa, H.S. *Handbook of Thin Film Materials: Deposition and Processing*, Academic Press, London, **2002**.
- [40] Cullity, B.D. *Elements of X ray diffraction*, Addison-Wesley Publishing Company, Inc., **1956**.
- [41] Cullity, B.D.; Stock, S.R. *Elements of X-Ray Diffraction*, 3rd ed., Prentice-Hall Inc., **2001**.
- [42] Handbook of Analytical Methods for Materials, Materials Evaluation and Engineering, Inc. (www.mee-inc.com).
- [43] Bruker Application Note #133: Introduction to Bruker's ScanAsyst and PeakForce Tapping AFM Technology (<http://www.bruker.com/products/surface-analysis/atomic-force-microscopy/modes/modes-techniques/primary-modes/scanasyst.html?gclid=CP7Ew9GU1r0CFQUJvAodfhkAbQ>)
- [44] Yasaka, M. X-ray thin-film measurement techniques: V. X-ray reflectivity measurement, *The Rigaku Journal*, **2010**, 26, Technical articles.

- [45] Ceriola, G.; Iacona, F.; La Via, F.; Raineri, V.; Bontempi, E.; Depero, L. E. X-Ray Reflectometry Study of the Structural Properties of SiO₂ and SiOF Thin Films, *Journal of The Electrochemical Society*, **2001**, 148, F221-F226.
- [46] Smith, B.C. *Infrared Spectral Interpretation: A systematic Approach*, CRC Press, **1999**.
- [47] Jellison, G. E. The calculation of thin film parameters from spectroscopic ellipsometry, *Thin Solid Films*, **1996**, 290-291, 40-45.
- [48] Fujiwara, H. *Spectroscopic Ellipsometry: Principles and Applications*; John Wiley & Sons Inc, **2007**.
- [49] Auciello, O.; Krauss, A.R. *In-Situ Real Time Characterization of Thin Films*, John Wiley & Sons Incorporated, New York, **2001**.
- [50] J. A. Woollam Co., Incorporated, *Guide to Using WVASE32 Spectroscopic Ellipsometry Data Acquisition and Analysis Software*, Copyright **1994- 2008**.
- [51] Cho, Y.J.; Nguyen, N.V.; Richter, C.A.; Ehrstein, J.R.; Lee, B.H.; Lee, J.C. Spectroscopic ellipsometry characterization of high-*k* dielectric HfO₂ thin films and the high-temperature annealing effects of their optical properties, *Applied Physics Letters*, **2002**, 80, 1249-1251.
- [52] Mukhopadhyay, A.B.; Sanz, J.F.; Musgrave, C.B. First-principles calculations of structural and electronic properties of monoclinic hafnia structures, *Physical Review B*, **2006**, 73, 115330.
- [53] Ho, M.-Y.; Gong, H.; Wilk, G.D.; Busch, B.W.; Green, M.L.; Voyles, P.M.; Muller, D.A.; Bude, M.; Lin, W.H.; See, A.; Loomans, M.E.; Lahiri, S.K.; Raisanen, P.I. Morphology and crystallization kinetics in HfO₂ thin films grown by atomic layer deposition, *Journal of Applied Physics*, **2003**, 96, 1477-1481.

- [54] Ramana, C.V.; Baghmar, G.; Rubio, E.J.; Hernandez, M.J. Optical Constants of Amorphous, Transparent Titanium-Doped Tungsten Oxide Thin Films, *ACS Applied Materials and Interfaces*, **2013**, *5*, 4659-4666.
- [55] Trager, F. *Springer Handbook of Lasers and Optics*, Springer-Verlag Berlin Heidelberg, **2012**, p262-264.
- [56] Park, J-W, Lee, D-K.; Lee, H.; Choi, S-H. Optical Properties of thermally annealed hafnium oxide and their correlation with structural change, *Journal of Applied Physics*, **2008**, *104*, 033521.
- [57] Aarik, J.; Mandar, H.; Kirm, M.; Pung, L. Optical characterization of HfO₂ thin films grown by atomic layer deposition, *Thin Solid Films*, **2004**, *466*, 41-47.
- [58] Mudavakkat, V.H.; Atuchin, V.V.; Kruchinin, V.N.; Kayani, A.; Ramana, C.V. Structure, morphology, and optical properties of nanocrystalline yttrium oxide (Y₂O₃) thin films, *Optical Materials*, **2012**, *34*, 893-900.
- [59] Martinez, F.L.; Toledano-Luque, M.; Gandia, J.J.; Carabe, J.; Bohne, W.; Rohrich, J.; Strub, E.; Martil, I. Optical properties and structure of HfO₂ films grown by high pressure reactive sputtering, *Journal of Physics D: Applied Physics*, **2007**, *40*, 5256-5265.
- [60] Kosacki, I.; Petrovsky, V.; Anderson, H.U. Band gap energy in nanocrystalline ZrO₂:16%Y thin films, *Applied Physics Letters*, **1999**, *74*, 341-343.
- [61] Wong, H. *Nano-CMOS Gate Dielectric Engineering*, CRC Press Taylor & Francis Group, LLC, Florida **2012**, p64-67.
- [62] Das, N.C.; Sahoo, N.K.; Bhattacharyya, D.; Thakur, S.; Kamble, N.M.; Nanda, D.; Hazra, S.; Bal, J.K.; Lee, J.F.; Tai, Y.L.; Hsieh, C.A. Correlation between local structure and

- refractive index of e-beam evaporated ($\text{HfO}_2\text{-SiO}_2$) composite thin films, *Journal of Applied Physics*, **2010**, *108*, 023515.
- [63] Al-Kuhaili, M.F.; Durrani, S.M.A.; Bakhtiari, I.A.; Dastageer, M.A.; Mekki, M.B. Influence of hydrogen annealing on the properties of hafnium oxide thin films, *Materials Chemistry and Physics*, **2011**, *126*, 515-523.
- [64] Filatova, E.; Sokolov, A.; Andre, J-M.; Schaefers, F.; Braun W. Optical constants of crystalline HfO_2 for energy range 140-930 eV, *Applied Optics*, **2010**, *49*, 2539-2546.
- [65] Vargas, M.; Murphy, N.R.; Ramana, C.V. Tailoring the index of refraction of nanocrystalline hafnium oxide thin films, *Applied Physics Letters*, **2014**, *104*, 101907.
- [66] Gallais, L.; Capoulde, J.; Natoli, J-Y.; Commandre, M.; Cathelinaud, M.; Koc, C.; Lequime, M. Laser damage resistance of hafnia thin films deposited by electron beam deposition, reactive low voltage ion plating, and dual ion beam sputtering, *Applied Optics*, **2008**, *47*, C107-C113.
- [67] Al-Kuhaili, M.F.; Saleem, M.; Durrani, S.M.A. Optical properties of iron oxide ($\alpha\text{-Fe}_2\text{O}_3$) thin films deposited the reactive evaporation of iron, *Journal of Alloys and Compounds*, **2012**, *521*, 178-182.
- [68] Stenzel, O. *The Physics of Thin Film Optical Spectra: An Introduction*, Springer-Verlag Berlin Heidelberg, Germany, **2005**.

Vita

Mirella Vargas was born in Martinez, California on November 28, 1988 and grew up in El Paso, Texas. Mirella enrolled into the dual-college credit courses while at Andress High School, after which she enrolled into The El Paso Community College to complete core classes for an engineering degree. Ultimately, transferring to The University of Texas at El Paso (UTEP). As part of her undergraduate career Mirella took an internship with Alcoa Howmet in Wichita Falls, Texas where she worked as a Process Engineer. She received a Bachelor of Science in Metallurgical and Materials Engineering in May 2012. Mirella continued forth for a Master's degree at UTEP. Throughout the course of her graduate degree Mirella took on a summer research assistantship at The Air Force Lab in Dayton, Ohio. Furthermore, she presented *Structure and Optical Properties of Nanocrystalline Hafnium Oxide Thin Films Made by Sputter-Deposition* at the 60th American Vacuum Society International Symposium & Exhibition in Long Beach, California. Mirella is the first author of the following publications: Tailoring the index of refraction of nanocrystalline hafnium oxide thin films, *Applied Physics Letters*, 2014, *104*, 101907 and Spectroscopic ellipsometry determination of the optical constants of titanium-doped WO₃ films made by co-sputter deposition, *Journal of Applied Physics*, 2014, *115*, 133511. Mirella is currently awaiting graduation on May 17th, 2014.

Permanent address: 10320 Blythe Dr.

El Paso, TX 79924-3132

This thesis was typed by Mirella Vargas.